2022

The Breakup of RP-2 Liquid Fuel Droplets in a Detonation Field

Daniel Dyson
University of Central Florida

THE BREAKUP OF RP-2 LIQUID FUEL DROPLETS IN A DETONATION FIELD

by

DANIEL DYSON
B.S. University of Central Florida, 2021

A thesis submitted in partial fulfillment of the requirements
for the degree of Master of Science
in the Department of Mechanical and Aerospace Engineering
in the College of Engineering and Computer Science
at the University of Central Florida
Orlando, Florida

Fall Term
2022

ABSTRACT

Experimentally obtained droplet breakup patterns are presented for RP-2 liquid fuel droplets in the environment behind a detonation wave. To the best of our knowledge, this data is the first of its kind to examine the fundamental interactions between detonation waves and an individual fuel droplet. The experiments presented here are expected to support the ongoing effort of creating accurate models of droplet breakup in a variety of environments, which in turn will lead to enhanced predictions of rotating detonation engine performance, improved safety considerations for facilities operating in hazardous conditions, and new knowledge in energetics, hypersonics, and explosion dynamics research. Detonations were produced inside a detonation tube using a gaseous mixture of hydrogen and oxygen while the fuel droplets were allowed to fall into the line-of-sight of a pair of windows used for high-speed shadowgraphy. Baseline conditions for the detonation include an initial temperature of 293 K, an initial pressure of 760 torr, and an equivalence ratio of 0.7. Conditions produced by the detonation wave include an estimated Weber number of 150,000 and a Mach number of 0.84 for droplets with an average diameter of 2.30 mm. Comparisons are made between the observed deformation of the droplet and the results of other experiments from the literature. Comparisons of droplet deformation are also made to predictions from the Taylor Analogy Breakup model. Attempts are made to characterize the effects of different parameters, including initial pressure, equivalence ratio, the introduction of diluents to the gaseous mixture, and droplet diameter. Furthermore, the breakup of water droplets in the same baseline conditions and the breakup of fuel droplets in a methane-oxygen detonation environment are also presented for comparison.

ACKNOWLEDGMENTS

I would like to thank my advisor, Professor Subith Vasu, for his continued support during my research career and for consistently presenting me with new and exciting challenges so that I can realize my potential as a researcher.

This work is also made possible by partial funding from AFOSR (FA9550-20-1-0268) and AFRL (FA8651-18-2-0005). I would also like to acknowledge funding from the University of Central Florida (UCF) Florida High Tech Corridor Council (FHTCC) for this effort.

I would like to thank Dr. Kyle Thurmond (now at Los Alamos National Laboratory) for helping me to push my limits, achieve many things I did not think were possible during my work on the detonation tube facility, and develop myself into a researcher. I would also like to thank my former colleagues, Artem Arakelyan and Jonnathan Ramirez, and my current colleagues, Nicolas Berube and Sydney Briggs, for their hard work and dedication to our efforts in conducting our experiments and performing data analysis, as I would not be able to present these experiments without their help.

TABLE OF CONTENTS

LIST OF FIGURES

LIST OF TABLES

INTRODUCTION

Detonation waves (DWs) are shock waves (SWs) that depend on the combustion of a compressible mixture providing high exothermic pressures and thermal energy for continuous propagation. Their dependencies exhibit a combination of detonation cell size, fuel-oxidizer ratios, rate of chemical reactions, wave speed, turbulence, etc. Much work has been done in investigating their complex behavior [1-4], simplifying their characteristics via the classical Chapman-Jouguet (CJ) conditions, and in creating methods for simulations [5, 6].

One interest driving DW research is its potential application for thermodynamic cycles with efficiencies greater than the more common Brayton cycle [7]. Particularly, rotation detonation engines (RDEs) have been a forefront of simulation research [8, 9] due to their advantages of continuous thrust operations with only a single detonation initiation. For RDEs, liquid fuel would be introduced as a stream of droplets or as an aerosolized spray in combination with a gaseous oxidizer to constantly energize the DW. Therefore, the combustion process of fuel droplets in a detonation environment needs to be investigated to generate accurate models for predicting the performance of these engines. The RDE can also potentially be adapted into a rotating detonation rocket engine which would provide similar efficiency boosts and remove complexities associated with current combustion methods for rockets [10]. Other applications of such knowledge include safety considerations to prevent the formation of DWs, hypersonics and understanding interactions with non-reacting (e.g., water) and reacting (e.g., rocket propellant) droplets at such extreme conditions, energetics and accurately modeling the complex interactions between the different combustion events, and explosion dynamics.

In the case of liquid fuel droplets, their combustion timescale ($\tau_{combustion}$) depends on a complicated arrangement of multiple timescales: droplet vaporization (τ_{vap}), air/fuel mixing (τ_{mix}), and reaction/ignition/heat release (τ_{react}). In simulating SW to DW transition and propagation of DWs, various approaches have been taken to model this crucial time scale $\tau_{combustion}$. Some researchers [11-13] have taken a chemical-diffusive approach, where the entire process of droplet combustion is simplified to a single tractable Arrhenius rate law; approaches such as genetic algorithms are used to fit the rate parameters and properties of the fuel-air mixtures (e.g., density, fuel mass fraction, activation energy, etc.) in concert to replicate macroscopic observables (e.g., DW CJ velocity, temperature rise, etc.). This approach is semi-phenomenological in that the final "fit" parameters are not the physicochemical properties of the material. Another approach [8, 14-16] is to subsume the chemistry into an expression for an ignition delay time, which is obtained empirically. In a third approach [17-19], the vaporization of the droplet is assumed to be the rate-limiting step, and heat is released at the same rate as the vaporization rate $\dot{m}_v$.

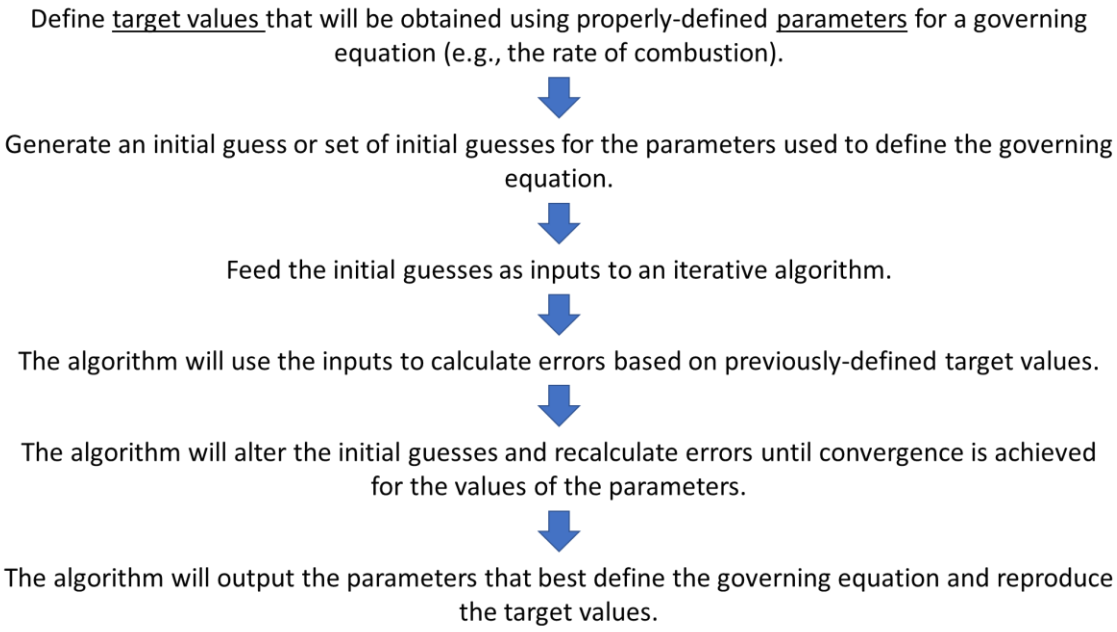

Figure 1: The general process used by some researchers to simulate combustion rates and time scales during a detonation event [11-13].

All these current approaches implicitly rely on untested assumptions/approximations and physicochemical models that are semi-empirical, extrapolated, and likely incorrect at conditions relevant to DWs. For example, the Taylor Analogy Breakup (TAB) model was developed to predict the displacement of the droplet equator over time as constant-velocity gas flows over the droplet (an example plot of the TAB model is provided as a comparison to the current experiments in the DISCUSSION section). As will be discussed in later sections, the foundations of this model and its derived constants originate from experiments considering SW interactions with droplets and therefore was not originally intended to be used for the extreme conditions experienced in detonation environments.

There are significant knowledge gaps at the scale of individual droplets or small clusters of droplets interacting with DW, which currently impede the construction of realistic and

accurate models of multi-phase detonations. In addition, models of droplet-DW interactions are not available, even for single droplets. This places severe limitations on understanding DW-droplet interactions and on developing physically correct models for drag, deformation, breakup, vaporization, and combustion.

Many previous experimental studies involved the use of imaging techniques to visualize interactions between droplets and SWs or DWs [20-24]. For example, Nicholls and Ranger [21] conducted fundamental studies on the interaction of SWs moving past water droplets using photographic techniques. In their study, they were able to characterize the deformation, displacement, and disintegration of water droplets as the convective flow following the SW (with shock Mach numbers in the range of 1.5-3.5) acted upon the droplets. They also derived a boundary-layer stripping model for the droplet disintegration phenomenon. They assumed that any disintegration of the liquid from the droplet's surface was purely due to the supersonic convective flow over the droplet. Ragland *et al.* [23] performed schlieren visualization on the propagation of DWs through an oxidizing atmosphere containing liquid fuel (diethylcyclohexane, or DECH) droplets. Their detonation tube was oriented vertically to allow the fuel droplets to fall through the length of the tube, and windows positioned along the tube provided optical access to capture DW propagation as well as the disintegration and combustion of individual drops by the DW. Later, they were able to show the DW propagating through sprays of fuel droplets had a velocity that was lower than the ideal CJ velocity for detonations in gaseous mixtures. Furthermore, the larger the size of each droplet in the spray, the slower the DW propagated through the spray [20]. These studies have been instrumental in providing fundamental data and information regarding the breakup of a (fuel) droplet due to a SW or DW.

Droplet breakup can be characterized by multiple different breakup mechanisms. Guildenbecher *et al.* presented a summary of regimes used in many previous papers on droplet breakup: vibrational, bag, multimode, sheet-thinning, and catastrophic breakup [25]. The Weber number (We) has historically been used to quantify the ratio of inertial forces on the droplet to the restoring forces due to the surface tension of the droplet and is also used to quantify the transitions between breakup regimes. For example, sheet thinning breakup is said to occur for the range of $80 < We < 350$, while catastrophic breakup occurs for $We > 350$ (these ranges apply for an Ohnesorge number, Oh, less than 0.1, where Oh is a nondimensional number describing the ratio of droplet viscous forces to surface tension forces) [25]. For reference, experiments employing SWs to induce droplet breakup yield values for We on the order of 10^3-10^4 or higher [26].

These breakup mechanisms were reclassified in recent literature as Rayleigh-Taylor Piercing (RTP) and Shear-Induced Entrainment (SIE), and they encompass the breakup modes that were previously thought to define droplet breakup [27-29]. In this recharacterization of breakup mechanisms, RTP houses the original modes of breakup found in low We flows: bag, bag-and-stamen, and multibag breakup modes. These modes are thought to stem from the Rayleigh-Taylor instability (RTI). SIE encompasses the higher We breakup modes: sheet thinning/stripping and any catastrophic breakup mode (the latter of which has been scrutinized for its existence, as current shadowgraph imaging techniques may be misrepresenting the surface waves which form on a droplet [27]). These breakup modes are assigned to the Kelvin-Helmholtz instability (KHI). These breakup modes are analyzed in great detail in [30], which also provides a detailed history of droplet breakup modes. These breakup modes may also be seen in DW-droplet interactions, but more research is needed to confirm their presence.

As it is clear, very few papers in the literature discuss the interaction between fuel droplets and DWs [8, 17] mostly due to the challenges in performing such experiments; therefore, new experimental investigations are clearly needed to understand these interactions. The ability to characterize this interaction further would have immediate applications to the development of RDEs [31], where the fuel would likely need to be stored and later ignited while in the liquid state. Furthermore, knowledge of the DW-fuel droplet interaction would better inform safety standards, have applications to hypersonics and related interactions, and enhance the field of energetics and explosion dynamics. This paper discusses preliminary results from a new experimental method that has been developed to obtain high-speed visualizations of the interaction between fuel droplets (in this case, RP-2) and a DW.

METHODS

Detonation Tube

The UCF detonation tube used in this study consists of a stainless-steel experimental section and dump tank separated by a thin aluminum diaphragm with a typical thickness of 0.02 inches or 0.5 mm, as shown in Figure 2. Before each experiment, the experimental section holds the hydrogen–oxygen (H_2-O_2) mixture, while the dump tank is initially at 1 atm. The purpose of the dump tank is to reduce any adverse effects from reflected DWs on equipment in the experimental section as well as mitigate interference of the reflected DWs with the droplet breakup event. The experimental section consists of a pre-detonator, a transition section, and finally the measurement section.

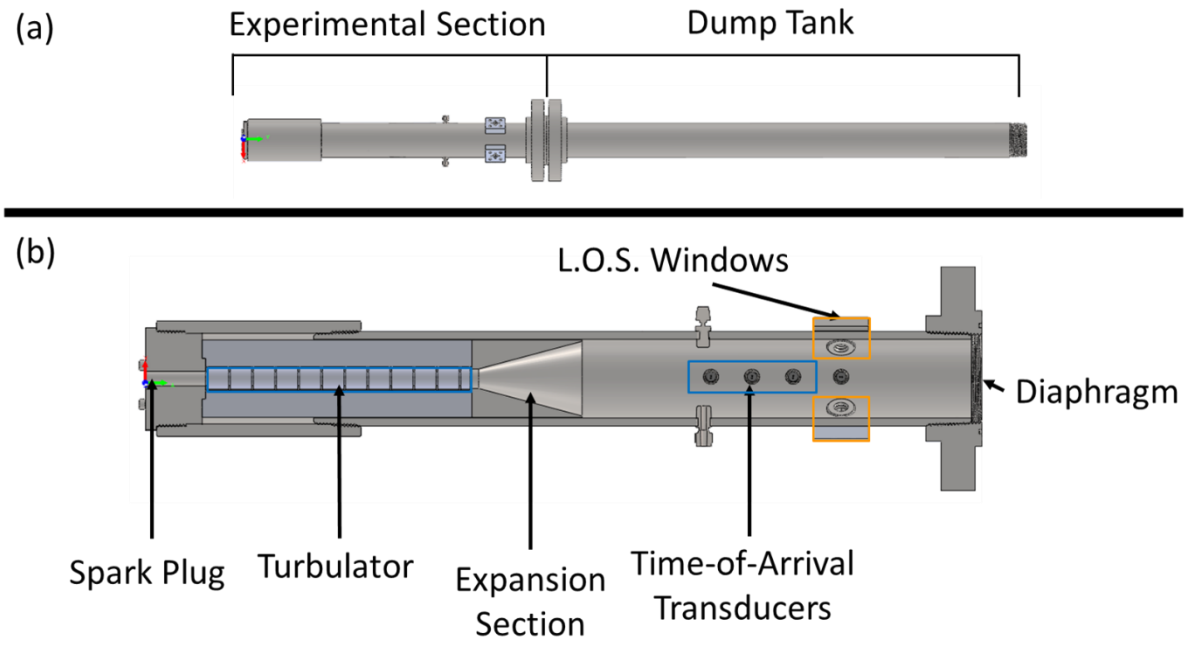

Figure 2: (a) UCF Detonation tube experimental section and dump tank. (b) Detonation tube experimental section breakdown.

The pre-detonator section, located at the most upstream end of the detonation tube, contains a spark plug which ignites the mixture to produce a subsonic flame or deflagration wave. The deflagration wave then passes through a Shchelkin spiral, or a “turbulator” (Figure 2), inside the pre-detonator, which consists of multiple evenly spaced obstructions to accelerate the deflagration wave and its combustion process by introducing turbulence. By the end of the Shchelkin spiral, an overdriven DW spontaneously results, concluding deflagration-to-detonation transition (DDT).

The overdriven DW then expands via the transition section to a larger cross-sectional area (7.36 cm diameter). The half angle expansion is 15º and has an expansion length of 10.16 cm (Figure 3). Because the DW is overdriven as it passes through the transition section, no decoupling between the leading shock and the combustion zone will occur, allowing the DW to propagate into the measurement section [32].

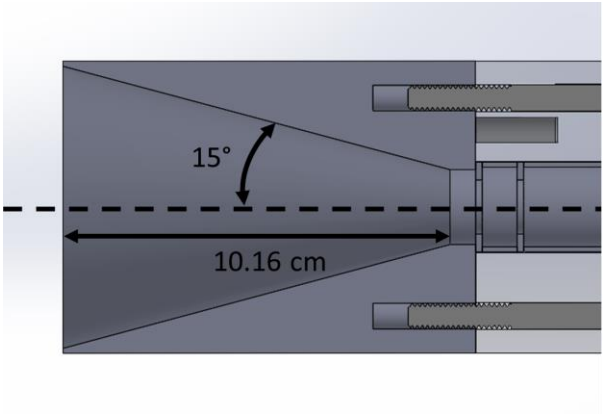

Figure 3: Transition section located at the downstream end of the pre-detonator. The half angle expansion is 15º and the expansion length is 10.16 cm.

At the measurement section, there are four ports spaced every 3.81 cm in the axial direction. The ports are located far enough away from the transition section such that the DW has

ample time to relax to a velocity that can be predicted from calculations of a CJ DW. At least two of the ports contain PCB piezoelectric pressure transducers sampling at 2.5 MHz to measure the DW velocity. PCB data was obtained using an NI PCI-6133 data acquisition device. This measured DW velocity is later compared to predictions calculated for a CJ DW [33] to verify that the measured DW was at the CJ state, allowing the assumption of other important parameters such as burned gas density, sonic velocity of the products with respect to the DW, and maximum pressure and temperature. The most downstream port is the location of the droplet introduction, and it is here that a pair of 1.27 cm diameter sapphire windows is located axially with the most downstream port.

After the experimental section has been filled to the desired pressure with a H_2-O_2 mixture, a fuel droplet is introduced to the experimental section. The liquid fuel is initially stored in a stainless-steel reservoir above the detonation tube. A high-pressure solenoid valve separates the liquid fuel reservoir from the experimental section, and it is allowed to open when creating the droplet. Once the solenoid valve is open, gravity will cause the liquid fuel from the reservoir to flow and eventually pool onto the tip of a 23-gauge needle within the experimental section. The droplet grows on the needle tip until the gravitational forces exceed the surface tension forces of the droplet, producing a droplet that falls from the needle. The resulting droplet is typically about 2.3 mm in diameter.

Baseline experiments were conducted which produced droplets with a mean diameter of 2.23 mm and a standard deviation of about 3% of the mean diameter. However, some experiments involved droplets with diameters as large as 2.8 mm and as small as 0.55 mm. Therefore, non-dimensional variables were used to account for differences in droplet diameter across experiments. These non-dimensional variables will be defined in later sections, and they

are shown to be useful in reducing the effects of initial droplet diameter on the observed droplet deformation.

Shadowgraph Imaging Setup

A schematic of the shadowgraphy imaging setup used during experiments is given in Figure 4. The free-falling droplet described in the previous section passes through the line-of-sight (LoS) of the sapphire windows, where an LED light source (100 mW, centered at 530 nm in wavelength) is directed through the experimental section. The droplet will reduce the amount of light transmitted from the light source to the other window. Therefore, a visible light detector is used to detect the drop in the light intensity, which leads to closing the solenoid valve, triggering DDT, and recording shadowgraphs of the droplet with the high-speed camera. The droplet moves about a fraction of a millimeter between the trigger time and the time when the DW arrives at the window in the experimental section; therefore, the droplet remains in the window during the time it takes to detect the droplet and trigger a detonation. The droplet's velocity as it falls is taken to be negligible compared to the droplet's velocity as it is entrained by the burned gas behind the DW (the droplet is observed to displace several millimeters within about 100 μs after the arrival of the DW).

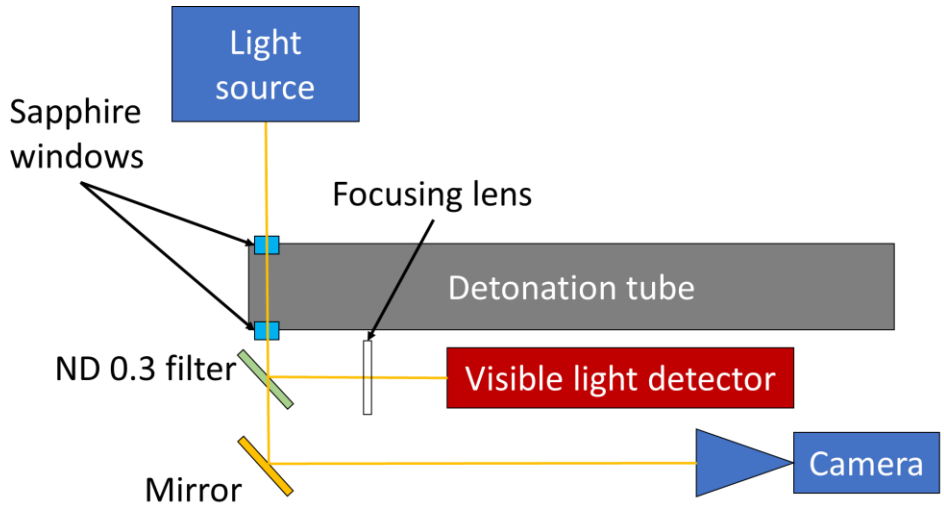

Figure 4: Schematic of the shadowgraphy imaging setup.

For the camera to record the droplet and for the visible light detector to detect the droplet in the same LoS, a neutral density filter (ND 0.3) is used to split the light into the camera and detector. The filter also helps to attenuate the light to the camera and prevents saturation of the images due to the intense light emitted from the DW. The light traveling to the visible light detector is then focused on the sensor using a lens.

The droplet breakup is recorded using the Photron FASTCAM SA-Z high-speed camera. The recording was performed at 160,000 fps, 0.0430 mm/pixel resolution, and a 0.16 μs exposure time. All triggering procedures and data collection were performed through an in-house LabVIEW program.

Limitations

Although conditions for a detonation flow field can be obtained for a liquid fuel droplet in our detonation tube, there are some limitations with the current experimental setup. The relatively short length of the pre-detonator and measurement sections lead to conditions where

high-speed flow behind the DW exists only briefly due to the limited volume of gas available which becomes accelerated by the DW event. As a result, the full droplet breakup cannot be captured (except for perhaps very small droplets), however the earliest stages of breakup are always captured. For this reason, only the first few frames of droplet breakup are examined and reported here.

The small size of the sapphire windows used for imaging (12.7 mm in diameter) also makes capturing the entire droplet breakup problematic. It is typical for a droplet to grow so much in size during breakup that parts of its features will extend beyond the frame of the window. In addition, the smaller the droplet the more likely the droplet will be displaced out of frame before the entire breakup process can be captured.

Finally, due to the intense light emitted from a DW and its products, the secondary combustion of the fuel droplet is "masked" by the DW. Efforts are currently underway to isolate the light emissions due to fuel droplet combustion from the light emissions due to DWs.

RESULTS

Description of Baseline Conditions

The baseline conditions used as a "control group" are the following: a mixture consisting of H_2-O_2 at an equivalence ratio of 0.7 with an initial temperature and pressure of 293 K and 760 torr was created to produce DWs in the current facility. These baseline conditions are used when comparing fuel droplet breakup characteristics as certain parameters are altered. A non-dimensional time will be used here to describe the timing of certain events observed during droplet deformation and breakup, and is defined as follows:

$$t^* = t\frac{V}{d_0} \quad (1)$$

Here, t is the elapsed time with respect to the approximate arrival of the DW, V is the estimated initial velocity of the burned gas with respect to the droplet, and d_0 is the initial droplet diameter. V remains constant for each time calculated, and because the droplet's velocity as it falls is taken to be negligible compared to the velocity of the burned gas, the value for u_g is only the velocity of the burned gas. Note that the velocity of the gas at the CJ plane of the DW was used in all calculations involving V, which corresponds to when the flow is choked due to heat addition from combustion and therefore at sonic velocity in the reference frame of the DW front. For a CJ DW, V is obtained by simply subtracting the sonic velocity from the DW velocity; a shift from the reference frame of the DW to the lab-coordinates reference frame is required to obtain the gas velocity at the CJ plane, which is explained in many combustion textbooks [34].

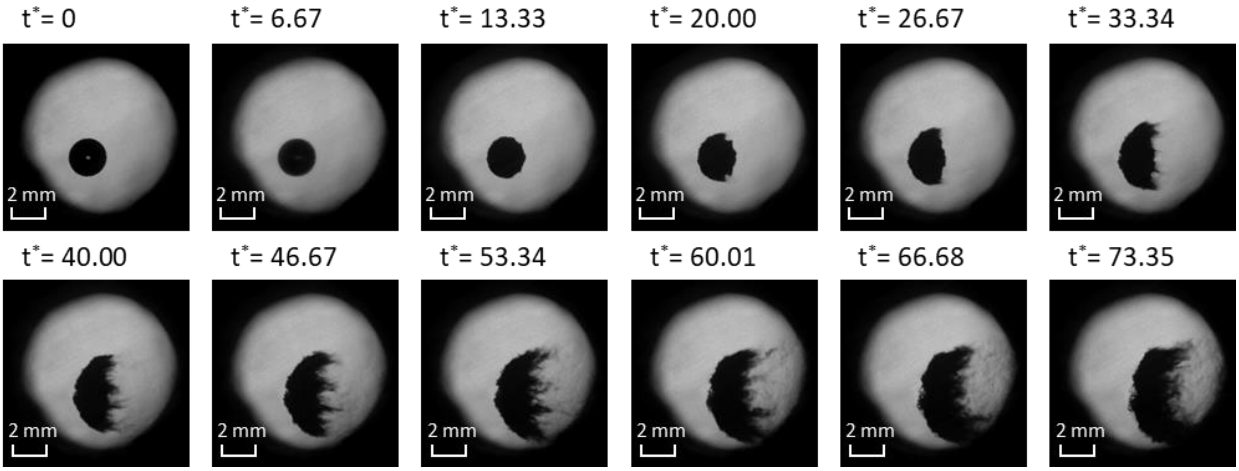

Figure 5: RP-2 droplet deformation in a detonation field at the baseline conditions. These images are the same as "Baseline 2" in APPENDIX B.

A description of the events detailing fuel droplet breakup at the baseline conditions will now be given. For convenience, example imagery is provided in Figure 5 to illustrate the series of events observed during a typical experiment. Initially, a droplet is introduced from a needle into the experimental section, such that it passes through the line-of-sight of the windows and therefore the camera. Then, the spark plug ignites sometime after and produces a DW via the DDT process, and the DW travels and meets the droplet. The DW itself does not immediately distort the shape of the droplet as it passes by the droplet. After the DW has passed, high-speed convective flow begins to act on the surface of the droplet.

On the windward surface of the droplet, very small surface waves begin to form ($t^* =$ 6.67) as the surface becomes disturbed from the step-change in relative velocity with the surrounding gas. Waves closer to the stagnation point of the droplet are assumed to be Rayleigh-Taylor (RT) instability waves [26]. Waves that form further away from the stagnation point but remain on the windward surface of the droplet have been identified previously as Kelvin-

Helmholtz (KH) waves, which arise due to the shearing action produced by the incoming gas flow on the surface of the droplet [29, 30]. Two rings of accumulated fluid begin to appear on the droplet's surface as well (t^* = 13.33), which likely arose due to the combined effects of migration and aggregation of the KH waves, and flow separation of the gas flow over the droplet which recirculates backward and pushes on the droplet fluid located on the leeward side [35]. The migration of KH waves and the recirculation effect will essentially pinch the droplet fluid into these ring structures.

The first ring is located near the equator of the droplet (i.e., the top and bottom if viewing the shadowgraphs such that the flow acts in the horizontal direction), and a second ring is located further downstream on the leeward side, between the first ring and the most aft portion of the droplet. The liquid-gas interface at the aft portion of the droplet appears to be distorted in such a way that a sharp point is produced at what would be the droplet's rear stagnation point, implying the existence of a conical feature here. The aft portion of the droplet then begins to deviate from this sharp point and instead flattens, while a fine mist darkens the area just downstream of the first ring of droplet fluid, hinting at the presence of droplet vapor (t^* = 20.00).

As time progresses, the first ring of liquid continues growing and extending downstream, so much so that it soon obscures the second ring due to the first ring having a larger diameter than the second ring (t^* = 26.67). Ligaments of droplet fluid, which appear as slender columns of fluid and mist, begin to appear and grow downstream of the droplet (t^* = 33.34). At this point, the droplet takes on the shape of a hemisphere in the shadowgraph images. This shape begins to dilate in the cross-stream direction while simultaneously shrinking in the streamwise direction (t^* > 33.34), though the streamwise length of the coherent portion of the droplet remains very

close in length to the droplet's initial diameter. In other words, the rate of enlargement of the droplet in the cross-stream direction outpaces the rate of shrinking in the streamwise direction.

Near the end of the experiment, the droplet morphs into a crescent moon shape ($t^* >$ 53.34). Its ligaments have grown only slightly but appear to dissipate some distance away from the leeward face of the droplet. The droplet has become quite thin in the streamwise direction while still lengthening in the cross-stream direction. The experiment officially comes to an end when the reflected DW passes over the droplet, reversing the flow direction and pushing the droplet out of view.

Detonation Wave Parameters

Table 1 shows the list of expected conditions produced in the detonation environment during experiments with the droplets. The measured values for We presented here are extremely high and therefore the breakup mechanism observed for all droplets is assumed to be SIE. This is supported by the current imagery obtained which shows stripping of fluid from the droplet surface and immediate transport of the fluid downstream and away from the core of the droplet.

Table 1: List of expected conditions produced in the detonation environment. Underlined parameters in the first row are the baseline conditions. Parameters that were altered are bolded for convenience.

P_1 (torr)	Fuel-Oxidizer Mixture Composition	Diluent & Diluent Proportion	ER	Droplet	Droplet size (mm)		DW speed (m/s)	Burned gas speed (m/s)	Burned gas density (kg/m^3)	Mach Number (M) of burned gas	Weber Number (We)	Ohnesorge Number (Oh)
<u>760</u>	<u>H_2-O_2</u>	<u>n/a</u>	<u>0.7</u>	<u>RP-2</u>	<u>2.30</u>		2555.68	1166.02	1.11	0.84	$150(10^3)$	0.00872
600	H_2-O_2	n/a	0.7	RP-2	2.30		2544.71	1161.44	0.88	0.84	$119(10^3)$	0.00872
800	H_2-O_2	n/a	0.7	RP-2	2.30		2558.05	1167.01	1.17	0.84	$159(10^3)$	0.00872
850	H_2-O_2	n/a	0.7	RP-2	2.30		2560.86	1168.18	1.24	0.84	$169(10^3)$	0.00872
760	**CH_4-O_2**	n/a	0.7	RP-2	2.30		2214.02	1019.09	2.14	0.85	$222(10^3)$	0.00872
760	H_2-O_2	**10% Ar**	0.7	RP-2	2.30		2363.74	1075.76	1.30	0.84	$150(10^3)$	0.00872
760	H_2-O_2	**20% Ar**	0.7	RP-2	2.30		2208.37	1001.98	1.49	0.83	$150(10^3)$	0.00872
760	H_2-O_2	n/a	**1.1**	RP-2	2.30		2918.34	1331.89	0.87	0.84	$154(10^3)$	0.00872
760	H_2-O_2	n/a	**0.5**	RP-2	2.30		2321.22	1057.12	1.30	0.84	$145(10^3)$	0.00872
760	H_2-O_2	n/a	0.7	**Water**	2.30		2555.68	1166.02	1.11	0.84	$48(10^3)$	0.00443
760	H_2-O_2	n/a	0.7	RP-2	**1.56**		2555.68	1166.02	1.11	0.84	$102(10^3)$	0.01058
760	H_2-O_2	n/a	0.7	RP-2	**0.55**		2555.68	1166.02	1.11	0.84	$36(10^3)$	0.01783

One of the most substantial factors in droplet breakup evolution is the initial diameter of the droplet. For example, when the droplet's initial diameter increases while keeping all other conditions constant, the time to breakup increases while the acceleration of the droplet decreases. In other words, increases in the initial diameter of the droplet slows down rates of deformation and displacement of the droplet. Therefore, an attempt has been made to normalize the deformation of the droplet with respect to the initial droplet diameter by defining non-dimensional displacements (see Taylor Analogy Breakup (TAB) Model) and non-dimensional times (see Description of Baseline Conditions), which are discussed in a later section. This procedure reduces the influence of the initial droplet diameter on the observed deformation of each droplet.

Initial Pressure

Although the droplets across each experiment tended to vary in initial diameter, two experiments were performed that produced very similar droplets in terms of initial diameters and will now be presented here.

Droplet breakup for RP-2 droplets was observed for initial pressures ranging from 600 torr to 850 torr. As the initial pressure of the fuel mixture inside the experimental section increases, the resulting DW peak pressure and burned gas density will also increase. The DW speed is also expected to increase, but the difference is minor.

Two experiments were selected for comparison in this section, where the first experiment used an initial fuel mixture pressure (P_1) of 850 torr while the second experiment used a P_1 = 600 torr. It should be noted that the experiment with P_1 = 600 torr was originally to be excluded from this paper because the measured DW speed had a deficit of about 4% with the expected CJ DW speed (typical uncertainties in the measured DW speed are about 2% for the current facility).

This suggests that the DW was slightly underdriven. However, the diameter of this droplet (2.03 mm) is very close in diameter to the droplet with P_1 = 850 torr (2.05 mm). Since the DW speed deficit is not excessive with respect to the expected CJ DW speed, a comparison between the droplets can be made.

The droplets for P_1 = 850 torr (left) and P_1 = 600 torr (right) are shown in Figure 6 for equivalent time steps (12.5 μs after the DW arrival). The differences between these droplets are rather subtle; both droplets share similar features of the rings of fluid forming near the equator and the deformation of the leeward surface. These minor differences in the droplet shape between both experiments suggests that the droplet deformation may be insensitive to this range of initial pressures.

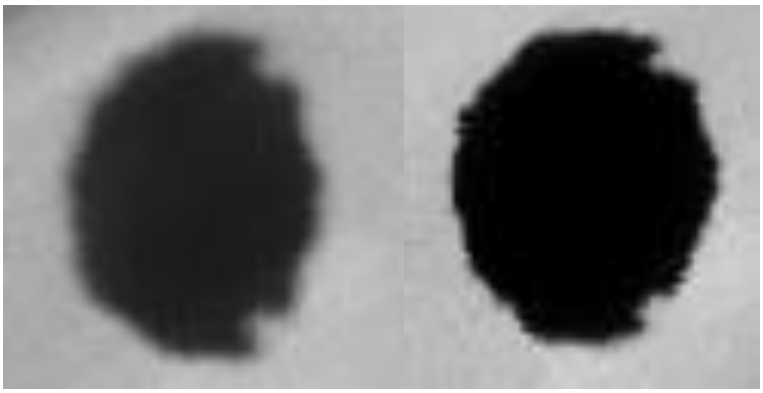

Figure 6: P_1 = 850 torr (left) and P_1 = 600 torr, DW speed deficit with CJ ~ 4% (right).

One difference that can be pointed out is regarding the shape of the leeward surface. For the higher initial pressure, the leeward surface is slightly more aligned with the vertical. Furthermore, the ratio between the cross-stream and streamwise diameters for P_1 = 850 torr appears to be slightly greater than for P_1 = 600 torr. This may suggest that for the higher initial pressure experiments, the stagnation pressure on the windward and leeward surfaces are larger,

causing a “sandwiching” effect on the corresponding surfaces. These stagnation pressure forces, which likely contribute significantly to deformation of the droplet, may be counteracting both the surface tension forces of the droplet and the static pressure at the equator of the droplet. On the other hand, the lower initial pressure experiment produces similar stagnation pressure forces, but these forces are reduced in magnitude and therefore do not deform the droplet as much as for the high initial pressure experiments.

DISCUSSION

Non-Dimensional Droplet Deformation

The non-dimensional displacement of the droplet equator versus the non-dimensional time was plotted for selected experiments from the current study. In other words, the growth of the droplet in the cross-stream direction was observed experimentally from the images, normalized with respect to droplet diameter, and plotted as a function of the non-dimensional time (see Description of Baseline Conditions). Note that the non-dimensional relationships employed are the same as those used for the TAB model, allowing for ease of comparison between experiments and model predictions. Comparisons with the TAB model and more detailed definitions of the non-dimensional variables will be discussed in the next section.

Ideally, the core of the droplet is to be considered when reporting the displacement of the droplet equator in the cross-stream direction. However, it is difficult to discern from the shadowgraphs alone where the core of the droplet exists and where the stripping of droplet fluid begins. Therefore, the reported measurements for the droplet diameter in the cross-stream direction extend to where a significant amount of droplet fluid exists in space, which may include ligaments of droplet fluid being carried away by the convective gas flow.

Plots of these non-dimensional variables were made for all baseline experiments (Figure 7). Again, the baseline experiments were run at conditions described in the first row of Table 1. There is reasonable agreement among each of these baseline experiments. This relationship appears to hold for varying droplet sizes; plotting one of the baseline curves (in this case, Baseline 3 from Figure 7) along with curves for droplets with reduced initial diameters appears to show similar agreement for essentially the same detonation conditions (Figure 8). Therefore,

the non-dimensional displacements versus non-dimensional time plots appear to be effective enough to warrant analysis across the different detonation conditions produced, even with variations in droplet diameter across each experiment.

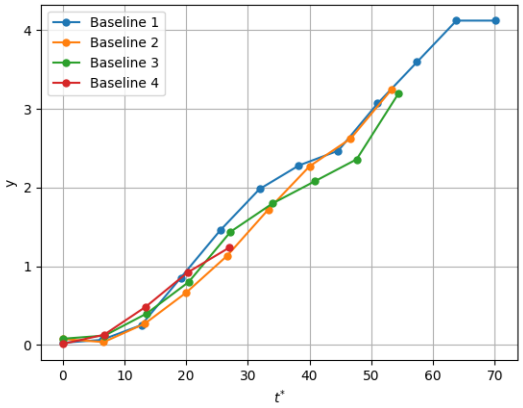

Figure 7: Non-dimensional displacement of equator versus non-dimensional time plots for the baseline experiments.

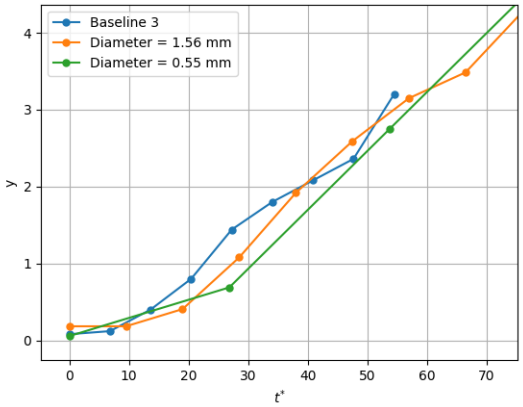

Figure 8: Non-dimensional displacement of equator versus non-dimensional time plots for one baseline experiment and two experiments involving reduced initial droplet diameters.

The plots of these non-dimensional displacements and times allow the current analysis to focus on cases where significant deviations from baseline occurred. It is interesting to note that for most experimental parameters investigated, the non-dimensional displacement of the droplet equators matched reasonably well with the baseline experiments. This may be most surprising for the water droplets, which had a surface tension of nearly three times that of RP-2, meaning a reduction of the We by a factor of 3 compared to baseline. The plot for the water droplet is shown in Figure 9, and images of its breakup are included in APPENDIX B: DROPLET IMAGES, which also contains images of droplet breakup for all other experiments.

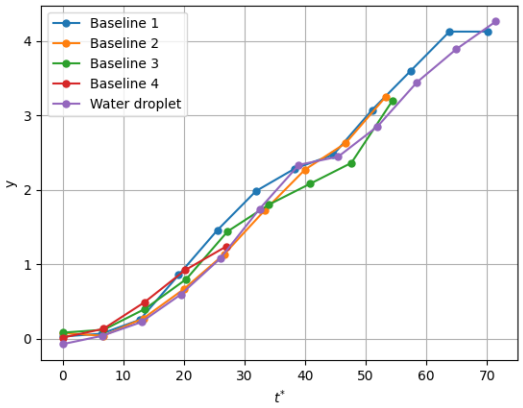

Figure 9: Non-dimensional displacement of equator versus non-dimensional time plots for the baseline experiments and one water droplet experiment with droplet diameter of 2.28 mm.

Methane Detonations

Droplets in a methane detonation field showed significant deviations from the baseline hydrogen detonations. For the experiments with methane detonations, individual droplets with diameters of 1.98 mm, 1.45 mm, and 1.02 mm were introduced. Again, comparing the observed non-dimensional displacements of their equators shows reasonably good agreement, though with some variability across the runs (Figure 10).

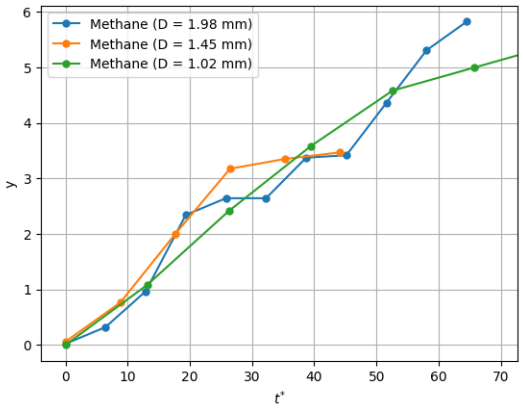

Figure 10: Non-dimensional displacement of equator versus non-dimensional time plots for the methane experiments.

The droplet with a diameter of 1.98 mm is compared to the baseline conditions (Figure 11), which shows that for the methane experiments the droplet equator is generally displaced more for all observed times than for the baseline experiments. This may be explained by methane producing more extreme detonation conditions than hydrogen; methane detonations produce an expected We of 222(10^3) for droplets 2.30 mm in diameter, which is greater than that for hydrogen detonations by nearly a factor of 1.5. The methane experiment most closely matching the baseline experiments is for the droplet with a diameter of 1.98 mm, which was calculated to have a We of 191(10^3). The results of the methane experiments show that normalization of droplets across different detonation environments may require either accounting for the increased influence of the expected inertial forces the droplet experiences or the heat release from the combustion, which are both determined by the chemical composition of the initial gas mixture sustaining the DW.

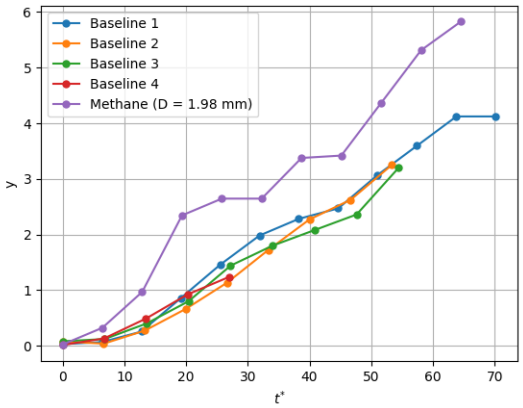

Figure 11: Non-dimensional displacement of equator versus non-dimensional time plots for the baseline experiments and one methane experiment with droplet diameter of 1.98 mm.

Upon observation of the plots for the baseline and methane experiments, it was noticed that the points for each experiment approximately follow a straight-line path for the entire sampled period (when examining only the earliest times, the growth rate does appear more parabolic or sinusoidal in nature, but for simplicity the entire experiment will be examined). If the baseline and methane experiments are plotted separately from each other, a simple linear regression analysis with the y-intercept set to zero yields best-fit model equations with r-squared values of 0.98 for each set of experiments. The slope of the curve fitting the methane experiments is greater than that for the baseline experiments by a factor of about 1.5.

Argon-Diluted Detonations

Droplet breakup experiments were conducted with the same baseline conditions for the gaseous mixture, but with 10% and 20% argon added to the gaseous mixture. For experiments where 10% argon was introduced as a diluent to the gaseous mixture, the observed displacement trends approximately followed the baseline trends. For experiments where 20% argon was

introduced, the observed displacement initially followed baseline trends up to $t^* \approx 10$ but then increased by up to 50% greater than the corresponding baseline displacement at the latest observed times of $t^* \approx 40$ (Figure 12). The droplet in Figure 12 had an initial diameter of 2.15 mm (see "20% Argon (3)" in APPENDIX B: DROPLET IMAGES), whereas two other experiments (plots not shown) had initial droplet diameters of 2.16 and 2.66 mm while still displaying the same approximate trend. Only one other experiment at 20% argon showed a trend (not shown) that aligned well with the baseline experiments (initial diameter = 2.51 mm. See "20% Argon (4)" in APPENDIX B: DROPLET IMAGES).

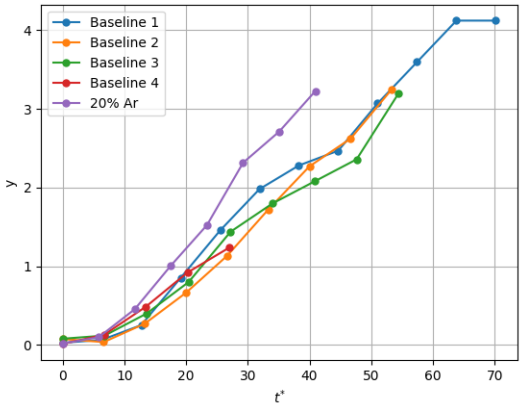

Figure 12: Non-dimensional displacement of equator versus non-dimensional time plots for the baseline experiments and one 20% argon experiment.

Comparing the initial detonation conditions with baseline, for 20% argon the burned gas speed is reduced by 14% while the density of the burned gas is increased by 34%. The reduction in gas flow speed and increase in gas density approximately negate each other when calculating the We for 20% argon experiments and for a droplet diameter of 2.30 mm. Another experiment was conducted with 20% argon for a droplet with an initial diameter of 2.66 mm and a calculated

We of about $170(10^3)$; however, the same trend was observed in its non-dimensional displacement over non-dimensional time. The observed deviation from baseline cannot be attributed purely to a change in We.

Due to the relative reduction in the concentration of oxidizing species, it follows that the reaction rate of the droplet has also been reduced. Therefore, less droplet mass is consumed by chemical reactions, which means that more droplet mass should be visible around the droplet (i.e., at the equator) than for experiments containing a greater abundance of oxidizer and therefore enhanced rates of combustion. This hypothesis is supported by current observation of the corresponding plots. This would also suggest that combustion of the droplet is occurring over the equator of the droplet, where the speed of the flow is expected to be near its maximum as it traverses the surface of the nearly (hemi-)spherical droplet. This is somewhat surprising because it was expected that a flame would not remain attached to the droplet when the gas speeds are expected to be so high (greater than 1,000 m/s). The surface of the flame (assuming one exists at the droplet equator) would have to be aligned very closely with the direction of the gas flow so that the gas flow direction is nearly coincident with the surface of the flame and therefore the normal component of velocity across the flame front is reduced enough to hold a flame to the droplet.

It is important to mention that the water droplet experiment ideally should have no chemical reactions occurring in the droplet vapors. However, it should also be noted that the calculated We for the water droplet was reduced by a factor of 3. Therefore, the inertial forces are reduced with respect to the surface tension forces of the droplet. It may be expected then that if the We were somehow increased to match baseline conditions for water, then the observed

displacement of the droplet equator would be expected to increase substantially, representing an "inert" case in terms of chemical reactions that would otherwise consume the droplet vapors.

Taylor Analogy Breakup (TAB) Model

The Taylor Analogy Breakup (TAB) model was used to make predictions for the evolution of a given droplet's diameter in the cross-stream direction over time. The TAB model is taken from [36], which presents a derivation for the model. The fundamentals of this model involve modeling the displacement of the equator of the droplet based on the dynamic equation for a mass-spring-damper system with an external force acting on the system. In this case, the forcing term is the drag force on the droplet due to external flow from behind the DW, the spring force is analogous to the surface tension of the droplet, and the damping force is analogous to the droplet's viscosity [36]. For convenience, the final equation and corresponding parameters used by [36] to model the non-dimensional displacement of the droplet's equator are presented below:

$$\boldsymbol{y = We_c + \exp\left(-\frac{t}{t_d}\right)\left((y_0 - We_c) * \cos(\omega t) + \frac{1}{\omega} * \left(\frac{dy_0}{dt} + \frac{y_0 - We_c}{t_d}\right) * \sin(\omega t)\right)} \quad \textbf{(2)}$$

$$\boldsymbol{We_c = \frac{C_F}{C_k C_b} We_r} \quad \textbf{(3)}$$

$$\boldsymbol{We_r = \frac{\rho_g V^2 r}{\sigma}} \quad \textbf{(4)}$$

$$\boldsymbol{\frac{1}{t_d} = \frac{C_d}{2}\frac{\mu_l}{\rho_l r^2}} \quad \textbf{(5)}$$

$$\boldsymbol{\omega^2 = C_k \frac{\sigma}{\rho_l r^3} - \frac{1}{t_d^2}} \quad \textbf{(6)}$$

$$\boldsymbol{y_0 = y(0)} \quad \textbf{(7)}$$

$$\boldsymbol{\frac{dy_0}{dt} = \frac{dy}{dt}(0)} \quad \textbf{(8)}$$

$$y = \frac{x}{C_b r} \quad (9)$$

For this set of equations, t is the elapsed time in units of seconds after the step-change in relative velocity of the surrounding gas with respect to the droplet (in this case, the amount of time after the DW has passed over the droplet), ρ is density in kg/m^3 (where a subscript "l" denotes liquid, and "g" denotes gas. ρ_l for RP-2 is 806 kg/m^3 and ρ_g is typically 1-2 kg/m^3), V is the initial relative velocity of the gas with respect to the droplet in m/s (typically around 1000 m/s), σ is the droplet surface tension in N/m (for RP-2, σ = 0.023 N/m), μ_l is the dynamic viscosity of the droplet in Pa·s (for RP-2, μ_l=0.001828 Pa·s), y is the non-dimensional displacement, x is the displacement in meters, and r is the initial droplet radius in meters (typically 0.001 m or 1 mm). For these set of equations, [36] also gives experimentally obtained values for the constants: $C_F = \frac{1}{3}$, $C_k = 8$, and $C_b = 5$. Note that the Weber number, We_r, is calculated using the droplet radius; therefore, We_r is not equivalent to the "We" reported for the current experiments (Table 1) because these Weber numbers were calculated using the droplet diameter. Furthermore, the TAB model's experimentally obtained values are based on previous SW experiments, yet the model is currently being applied to conditions that extend beyond the originally intended range of We. Therefore, it is expected that there will be significant deviations in the experiments from the TAB model.

An example comparison of the TAB model to a baseline experiment is shown in Figure 13. Applying the TAB model to the baseline conditions of the current experiments shows that the TAB model generally underpredicts the growth rate of the displacement in the cross-stream direction by up to a factor of 2.5 for the latest times. This may be due to the method used to experimentally measure the displacement of the droplet, which may include ligaments or

fragments of droplet fluid migrating to the equator during droplet deformation, thereby biasing the measured displacements toward higher values than intended. Alternatively, this observation may indicate that another relationship exists that can more accurately predict the droplet equator displacement than the TAB model alone. It should be noted that the TAB model was developed partly on an experimentally obtained critical We of approximately 6 for droplet breakup in shock wave environments [36]. This may be one key factor that explains the difference between observed droplet diameters and the predicted diameters from TAB.

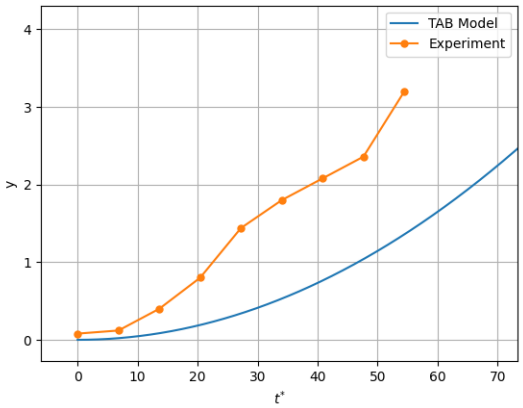

Figure 13: Comparison of the TAB model to "Baseline 3" experiment.

Another potential explanation stems from the statement by [37] that the surface tension of a liquid fuel droplet in a combustion environment will decrease substantially due to elevated temperatures and pressures, causing the surface of the droplet to approach its critical point. Recalling the fundamental concepts of the TAB model qualitatively shows that as the surface tension (analogous to the spring force in the mass-spring-damper system) decreases, the restoring force that attempts to bring the droplet back to a spherical shape also decreases. As a result, the droplet may be allowed to expand to even greater diameters than can be predicted from the TAB

model, which again is based on the results of shock experiments that typically produce post-shock temperatures and pressures much less than DW temperatures and pressures.

However, attempting to decrease C_k or the inputted droplet surface tension does not appear to change the TAB model. The only parameter of the TAB model that can be altered to produce better agreement is C_F, which directly influences the predicted growth rate of the displacement. Since the constant C_F is related to the forcing term (i.e., the drag force on the droplet), then there may be a relationship that exists between this constant and the inertial forces acting on a droplet (e.g., We). This suggestion is supported by observations from the previous section, where it was found that for droplets in a methane detonation field (and therefore an environment with a higher We), the displacement of the droplet equator was higher for all times compared to the baseline hydrogen detonation fields.

Rayleigh-Taylor Instability

A comparison between predicted and observed RT instability waves on the windward surface of a given droplet is performed, which is derived from the analysis detailed and presented by Joseph *et al.* [26]. This analysis involves calculating a theoretical value for the wavelength of RT waves located on the windward surface of the droplet, followed by a comparison to the observed wavelengths in the shadowgraph images of the droplet. It should be noted that this analysis is limited by constraints on our spatial resolution of the images; the predicted wavelengths are often of the same order of magnitude as our measured spatial resolution.

The main inputs for this RT analysis include the droplet's properties (density, surface tension, and viscosity) and a measured initial acceleration of the droplet. The acceleration of the droplet was measured using a MATLAB code, which tracks the position of the leading edge of

the droplet across each frame of the shadowgraph videos while also calculating the displacement across consecutive frames. Due primarily to the limited temporal resolution of the videos and the tendency for the droplet to move only a few pixels at a time, the uncertainty of such displacement measurements is quite high. Furthermore, this uncertainty is expected to propagate significantly in subsequent velocity and acceleration measurements of the droplet. Nevertheless, typical initial acceleration measurements for the current experiments are found to be of the order of 10^6 m/s^2, which is 1-2 orders of magnitude higher than the reported initial accelerations of Joseph *et al.* (10^4 - 10^5 m/s^2). Considering that the DW has a much higher Mach number (~5-7) than the reported SW Mach numbers from Joseph *et al.* (2-3) while realizing that the droplets between experiments are similar in properties and size, we can assume that the measured initial accelerations for the current experiments are valid.

An RP-2 droplet from one of the baseline experiments is shown to have surface waves near the droplet's stagnation point on the leading surface (Figure 14). Some of the observed wavelengths appear to be much longer than what Joseph *et al.*'s theory predicts for the current experiments. As stated previously, the droplet's effective surface tension is potentially much lower than anticipated because of the elevated temperatures the droplet experiences in the detonation field. A reduction in surface tension means that the corresponding Oh will increase and therefore the reported value for Oh (which is based on the surface tension of RP-2 at room temperature) may not be a good approximation. A substantially increased value for Oh has the effect of shifting the transitional We between breakup regimes, such that breakup mechanisms expected for low-We flows may now occur at higher We flows (if $Oh > 0.1$) [25]. The effect of an increased value for Oh is also observed in the predictions for RT wavelengths, where in Joseph *et al.*'s predictions the expected wavelength increases as the viscosity of the droplet

increases for the same SW conditions (increasing the viscosity of the droplet will also increase Oh) [26].

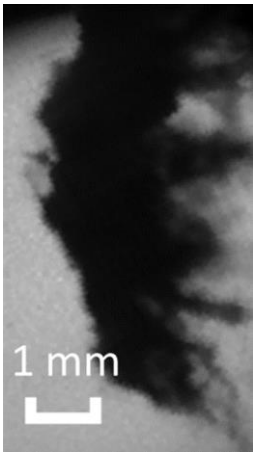

Figure 14: RP-2 droplet from Baseline 3 experiment. Surface waves are visible on the droplet's leading surface and in some cases appear to have longer wavelengths than theoretical predictions.

Therefore, since the RP-2 droplet may have a higher Oh, then it is expected to match closer to experiments with similar We flows but at the higher Oh. However, Joseph *et al.*'s theory predicts that the wavelengths will increase with an *increase* in surface tension for the current experiments and droplets, which contradicts expectations in terms of the effects of Oh alone. An explanation for this is that a reduced surface tension not only increases Oh, but also increases We. Therefore, the increases in both dimensionless numbers are competing. As surface tension approaches zero, the growth of We is expected to outpace that of Oh because observation of their definitions shows that $We \propto \sigma^{-1}$ while $Oh \propto \sigma^{-\frac{1}{2}}$, so droplet breakup mechanisms expected for high-We flows should be expected for droplets in the combustion environment. In other words, Oh may not be an important indicator in terms of the qualitative droplet breakup characteristics.

More data may be needed to investigate exactly how the surface waves are affected by variations in surface tension, viscosity, We, and Oh in detonation fields. Furthermore, it may be more suitable to have imaging of a cross-section of the droplet, which would eliminate the overlap of waves all along the leading surface of the droplet and allow for more reliable measurements of the surface waves [27].

CONCLUSION

Experiments involving DW interactions with RP-2 fuel droplets have been recorded using high-speed shadowgraph imaging. The breakup mechanism of these droplets appears to demonstrate an SIE breakup mechanism as expected for the extremely high Weber number flows observed in these experiments. Experiments were conducted by defining baseline conditions for the droplet breakup event followed by altering one condition at a time to observe its effect on the resulting droplet breakup.

Nondimensional variables describing the deformation of the droplet over time were defined. For most of the experiments, the nondimensional deformation plots appeared to approximately collapse to a single curve, which may suggest that the droplet breakup event in its earliest stages is relatively insensitive to the range of conditions imposed in the current experiments. The main factors influencing droplet breakup rates for the presented detonation conditions appear to be the chemical composition of the gas mixture that initiates and sustains the DW (i.e., using a methane mixture instead of a hydrogen mixture produced different droplet breakup characteristics) and the introduction of diluent gases (e.g., argon).

The effects of methane on droplet deformation were expected since the methane detonations produced higher Weber number conditions, which resulted in increased deformation rates in the droplet. As for detonations employing argon as a diluent, the increased deformation rates may be explained by a lack of chemical reactions of the droplet vapors, resulting in less droplet mass being consumed by combustion and an apparent increase in droplet deformation. It would be interesting to examine more closely the competition between the apparent rate of displacement of the fuel droplet's equator and the rate of consumption of the fuel from the

surface of the droplet. Obviously, combustion of the fuel droplet plays an important role in the morphology of the droplet in a detonation field and should be investigated more closely in future experiments.

Also, the experimental nondimensional plots were compared to the TAB model for droplet deformation, and in all experiments the observed deformation occurred at a higher rate than predicted by the TAB model. This is likely explained by either the technique used to measure droplet deformation, which may have unintentionally included fragments of droplet fluid migrating to the equator, or the derivation of the TAB model which is based on empirical data originating from less intense, SW-induced flows.

Finally, a brief comparison was made in terms of RT surface waves between the current droplets and droplets from the literature. Even though the conditions between each are very different (detonation flow field vs SW-induced flow field), the surface waves observed in each are qualitatively similar. An explanation for this may be due to the reduction in surface tension of the droplet in the detonation field which has the effect of increasing Oh. However, a reduced surface tension also increases We at a faster rate, so a more careful analysis is required to study how local droplet conditions would influence the resulting breakup in a detonation environment.

Future work will involve more diagnostics investigating the combustion characteristics of the fuel droplets, including laser absorption spectroscopy and emission measurements of target chemical species unique to the combustion of the droplet. Such diagnostics would grant the ability to correlate droplet breakup characteristics (e.g., deformation rates and shapes, breakup times, etc.) to observed combustion characteristics (e.g., ignition delay times, burning rates, etc.).

APPENDIX A: EXPERIMENTAL UNCERTAINTIES

Several experimental uncertainties were calculated, the most relevant uncertainties will be presented here. For all experimental uncertainties, the following uncertainty propagation equation was generally used:

$$u = \sqrt{\sum \left(\frac{\partial F}{\partial X_i} u_i \right)^2}$$

u represents the uncertainty of a variable, F is the equation used to calculate for the value of a variable, X is an experimentally measured value used in the equation F, and u_i is the uncertainty of the experimentally measured value X.

The DW velocity is calculated with the following equation:

$$V_{DW} \equiv F = \frac{\Delta x}{\Delta t} = \frac{x_2 - x_1}{t_2 - t_1} = \frac{x_2 - x_1}{n_2 - n_1} f_s$$

x denotes the location of each of the two time-of-arrival pressure transducers used to detect the arrival of the DW, n denotes the sample number corresponding to the arrival of the DW, and f_s is the sampling rate of the pressure transducers (2.5 MHz for the current experiments). Subscripts "1" and "2" denote the upstream and downstream pressure transducers, respectively.

The uncertainty in x is determined directly by the machining tolerances on the locations of the ports containing the pressure transducers on the detonation tube, which were reported to be 0.381 mm. The uncertainty in n is assumed to be purely due to resolution, or more specifically, half the resolution. When expressed as the number of samples, the uncertainty in n is simply one-half of a sample. Finally, by taking the partial derivative of F with respect to each of the measured values (x_1, x_2, n_1, n_2) and substituting the corresponding expressions for all partial

derivatives and uncertainties in the measured values, a final uncertainty for the measured DW speed can be obtained.

An example calculation of the DW speed uncertainty will now be provided. For the Baseline 1 experiment, 37 samples were counted between the arrival of the DW at each pressure transducer (equivalent to 14.8 μs of elapsed time) separated by a distance of 3.81 cm, resulting in a measured DW speed of 2574 m/s. With the sampling frequency and the positions of the pressure transducers, along with the uncertainties in the sample count and pressure transducer locations, the uncertainty of the DW speed can be calculated. In general, the partial derivatives of F can be written as:

$$\frac{\partial F}{\partial x} = \frac{1}{\Delta t}$$

$$\frac{\partial F}{\partial n} = \frac{V_{DW}}{\Delta n}$$

When the partial derivatives are taken with respect to each measured value (x_1, x_2, n_1, n_2), the resulting expression may have a negative sign, however this has no effect on the final calculation of the uncertainty due to the product $\frac{\partial F}{\partial X_i} u_i$ being squared in the equation for uncertainty propagation. Substituting all known values into these expressions and solving the uncertainty propagation equation, a final uncertainty of 61 m/s (2%) is calculated for the measured DW speed.

To illustrate how this uncertainty is used, note that for the Baseline 1 experiment, the CJ DW speed is expected to be 2556 m/s given the initial gaseous mixture composition, according to calculations from SDToolbox [33]. By comparison of this expected value and the measured DW speed, the expected value is within the uncertainty of the measurement by simply

subtracting the measured DW speed by the calculated uncertainty to obtain a lower limit value and observing that the expected value falls between the measured value and the lower limit value. This verification that the measured DW speed is indicative of a CJ DW allows us to then assume a variety of post-detonation conditions.

The gaseous mixture composition also has uncertainty, so it is important to know its uncertainty to ensure the DW generated from the mixture corresponds to the reported mixture composition. The most important parameter of the mixture composition is arguably the ER of the mixture. To calculate the ER (F) and its uncertainty (u), the measured values (X) used are the partial pressures of fuel and oxidizer, P_i. When the mixture is initially formulated, the method of partial pressures is used to introduce the required proportions of fuel and oxidizer, and is illustrated by:

$$P_i = \chi_i P_{tot}$$

P_i is the partial pressure of a particular gas (e.g., fuel), χ_i is the mole fraction of the gas, and P_{tot} is the total pressure of the mixture. χ_i may be calculated for both fuel and oxidizer by dividing the respective number of moles of the gas (e.g., fuel) by the total number of moles in the mixture. The moles of fuel and oxidizer are found using the balanced chemical equation for a combustion reaction between fuel and oxidizer at any desired ER.

The ER is defined as:

$$ER \equiv F = \frac{\frac{N_f}{N_o}}{\left(\frac{N_f}{N_o}\right)_{st}} = \frac{\frac{\chi_f}{\chi_o}}{\left(\frac{\chi_f}{\chi_o}\right)_{st}} = \frac{\frac{P_f}{P_o}}{\left(\frac{P_f}{P_o}\right)_{st}}$$

N is the moles of the corresponding constituent gas. Subscripts "f" and "o" are used to denote fuel and oxidizer, respectively. The subscript "st" refers to the stoichiometric combustion of the fuel and oxidizer (when ER = 1) and is effectively a constant when the fuel and oxidizer types are fixed (e.g., hydrogen and oxygen). The ER can be written in terms of either moles, mole fractions, or partial pressures by realizing that each is directly proportional to each other.

With F defined, partial derivatives can easily be taken with respect to the measured P_f and P_o when making the mixture. Uncertainties for P_f and P_o are obtained from the equipment used to measure the pressure, including uncertainties due to resolution, and reported "reading" uncertainties. Also, since the creation of a mixture involves reading *cumulative* pressures, there is uncertainty propagation that occurs from having to measure the pressure of fuel and oxidizer combined, followed by subtraction of the measured fuel partial pressure to obtain the oxidizer partial pressure. Finally, an observed ER and a corresponding uncertainty can be found, and for all experiments the uncertainty range for the ER always captured the reported ER.

The droplet size has uncertainty primarily due to the camera's spatial resolution and how it was calibrated. To calculate the droplet diameter (F) and its uncertainty (u), the measured values (X) used are the number of pixels spanning across the diameter of the approximately spherical droplet (D_{pxl}) and the camera calibration constant (C) expressed in units of mm/pxl:

$$D \equiv F = D_{pxl}C$$

The uncertainty in D_{pxl} is simply one-half of a pixel. The uncertainty in C depends on a reference length used when calibrating the camera. In this case, an object of known length is carefully positioned at the location where the droplets are expected to fall into the experimental

section. The camera can then observe this object and calculate C based on the number of pixels spanning across the object in the image. The length of the object is determined by calipers, which had a resolution of 0.02 mm, so the uncertainty of the length of the reference object was also accounted for using uncertainty propagation.

Again, partial derivatives can be found for F with respect to each measured value (D_{pxl} and C). Substituting the partial derivatives and individual uncertainties into the uncertainty propagation equation, an uncertainty for any measured length in the camera frame can be found. For Baseline 1, the droplet diameter was measured to be 2.32 mm and its corresponding uncertainty was found to be +/-0.025 mm (about 1% of the measured diameter).

The uncertainty propagation method was also applied to all reported dimensionless numbers. We calculations had typical uncertainties of about 10%, Oh about 0.5%, and Ma about 5%. The reason for the relatively high uncertainty in We is likely because of the effect of squaring the velocity in definition. This means that small uncertainties in velocity will result in larger uncertainties in the We. The velocity used in We is directly proportional to the measured DW speed, so reducing the uncertainty in the measured DW speed (e.g., by increasing the sampling rate) would likely reduce the uncertainty in We. Also, it should be noted that uncertainties for some properties, such as surface tension, viscosity, and density of the droplet, have been neglected in these uncertainty calculations.

APPENDIX B: DROPLET IMAGES

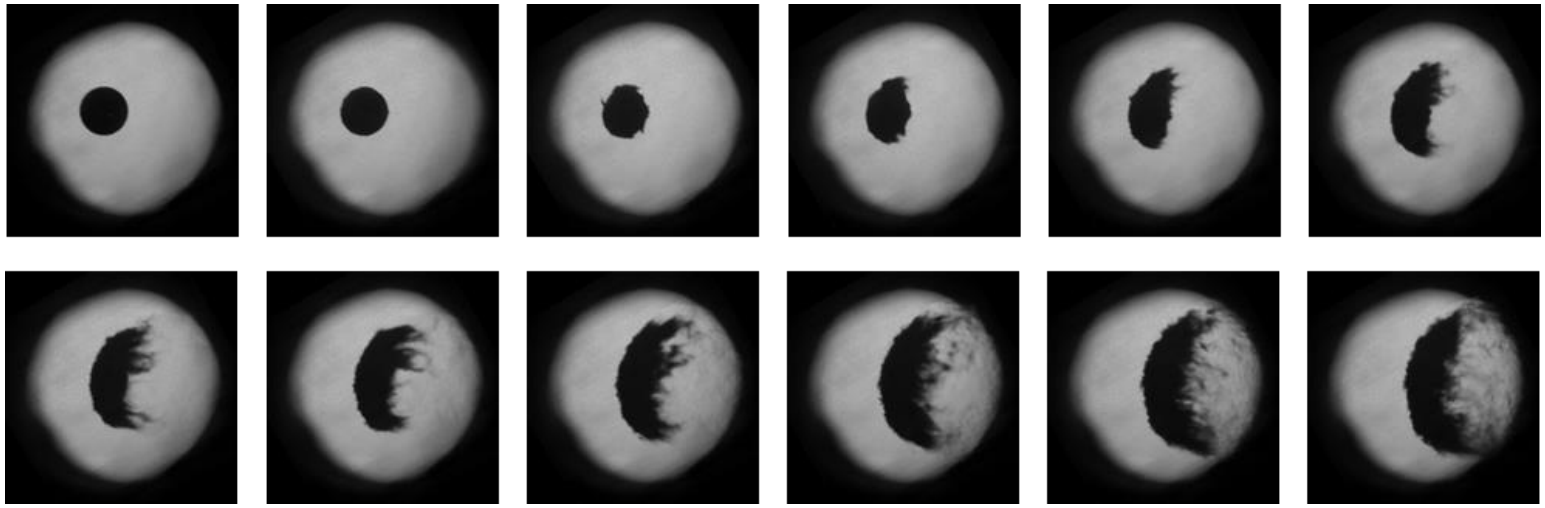

Baseline 1

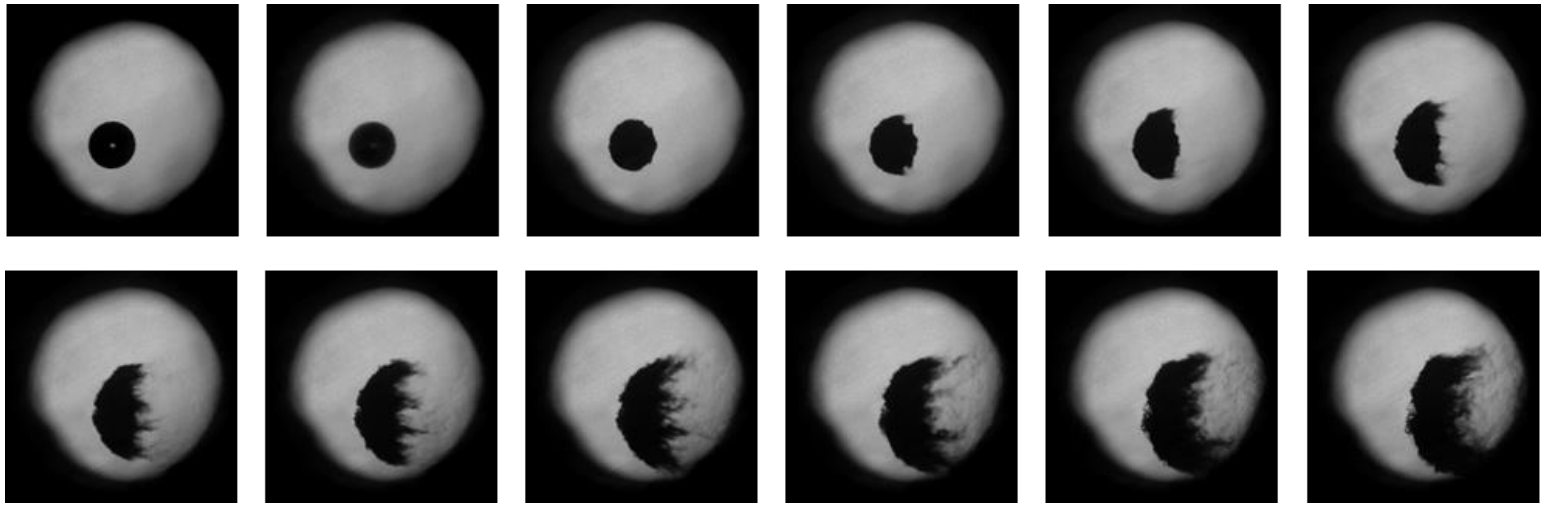

Baseline 2

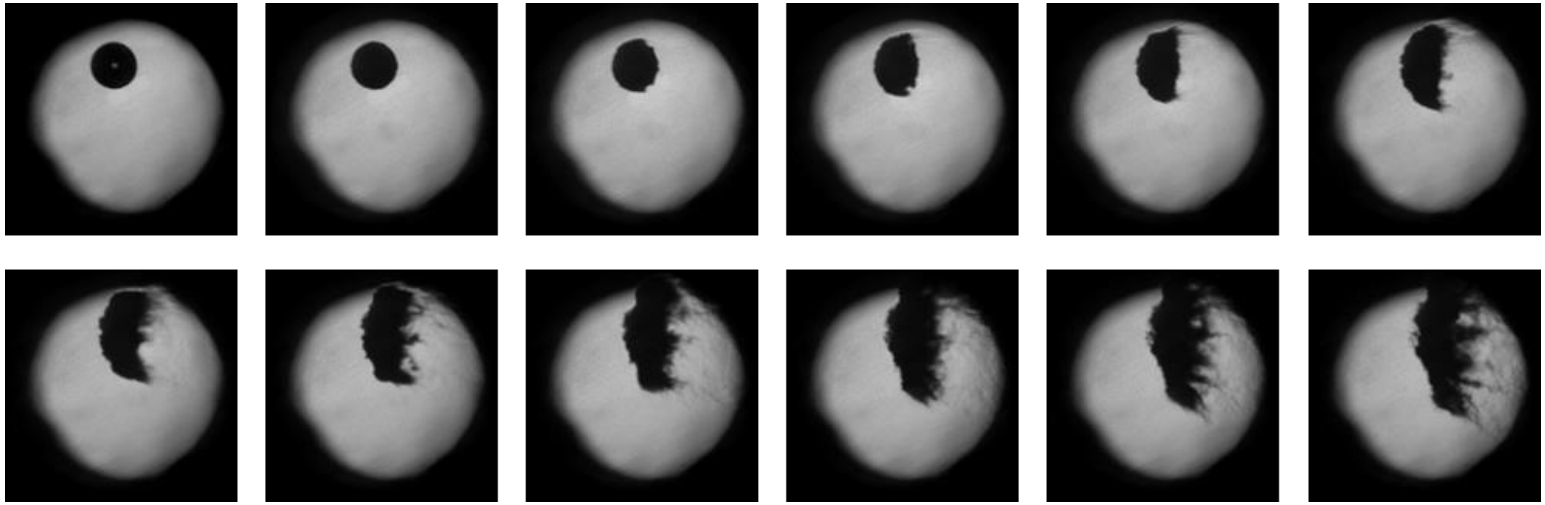

Baseline 3

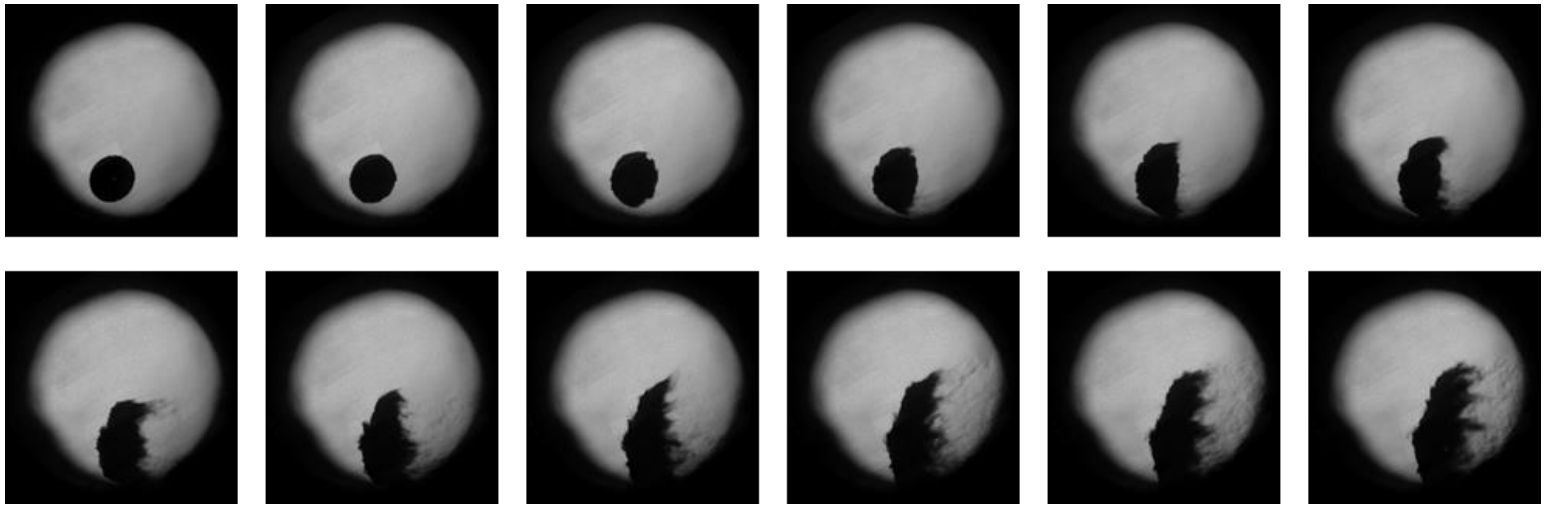

Baseline 4

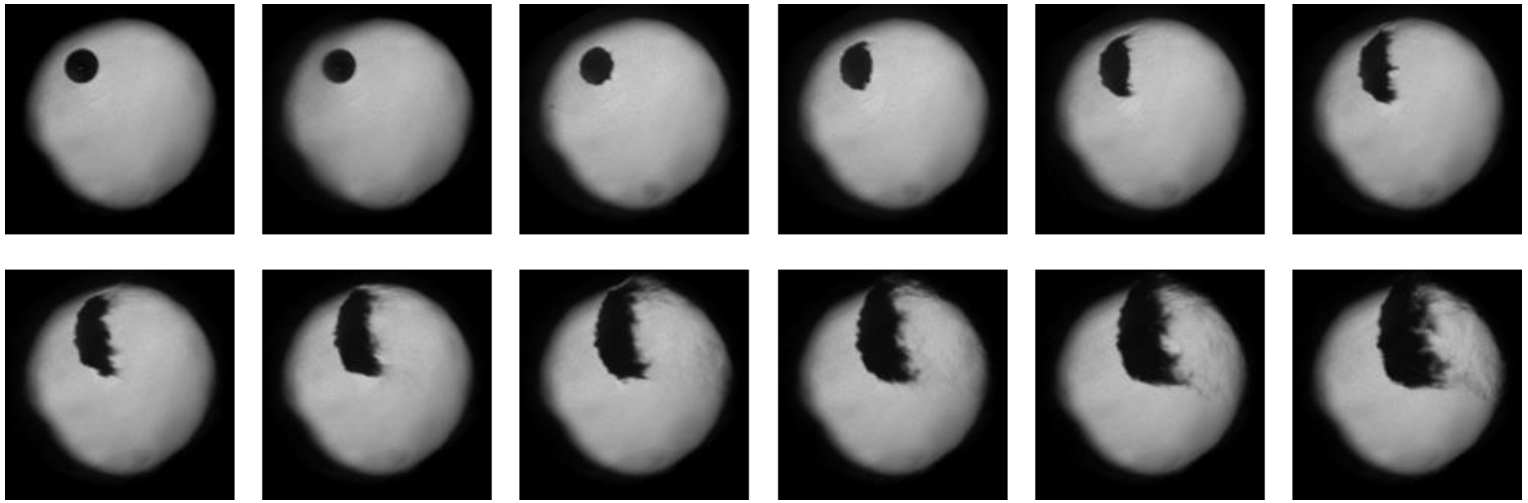

Diameter = 1.56 mm

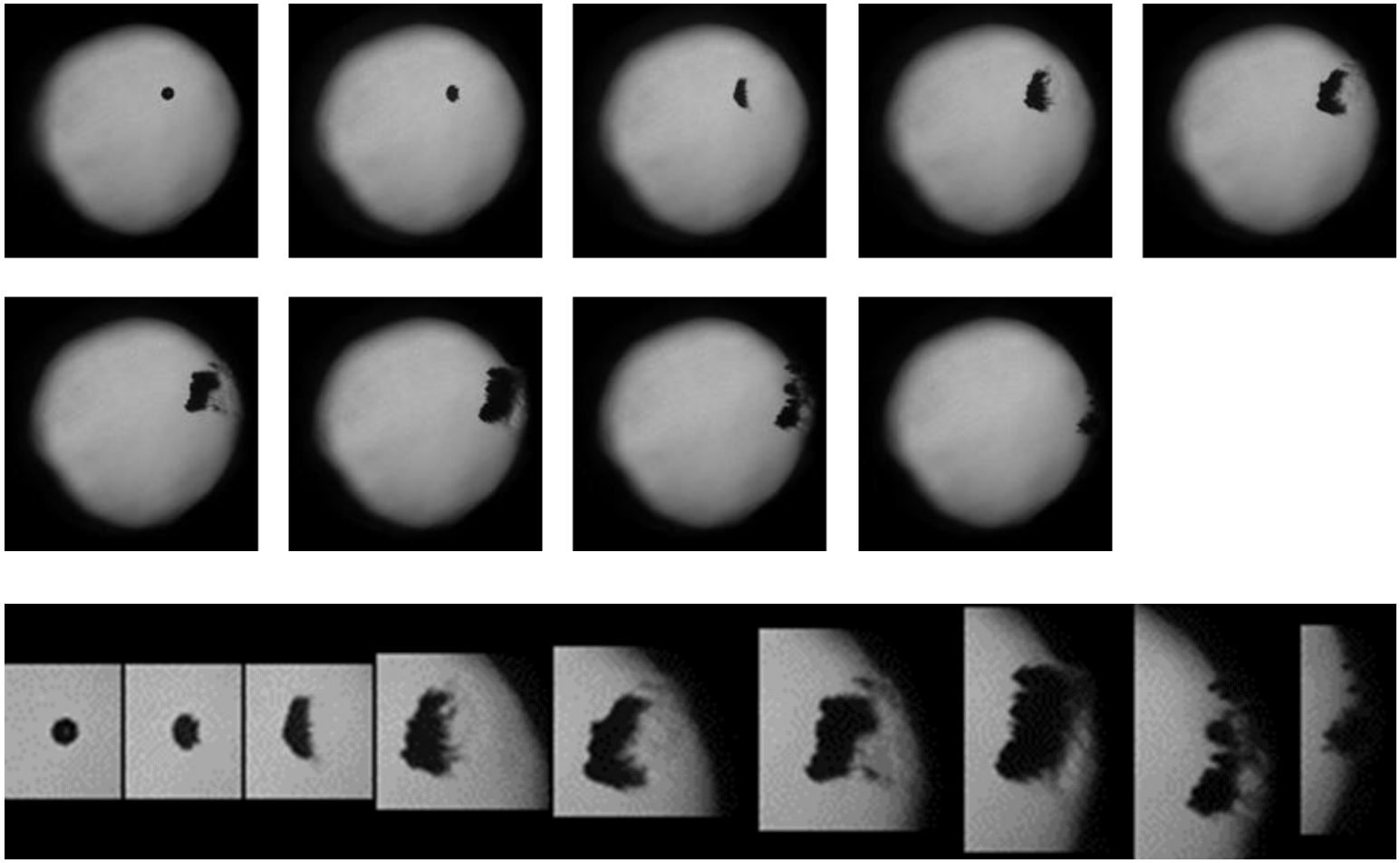

Diameter = 0.552 mm. The bottom row is a zoomed-in view of the same droplet above.

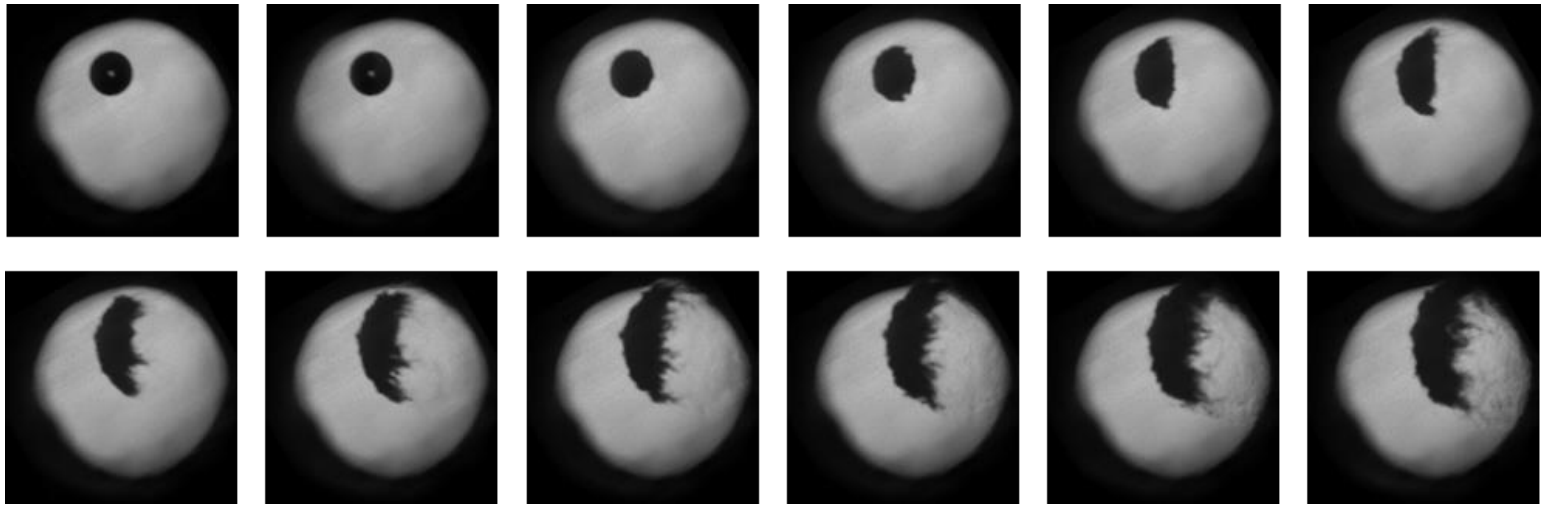

P_1 = 850 torr

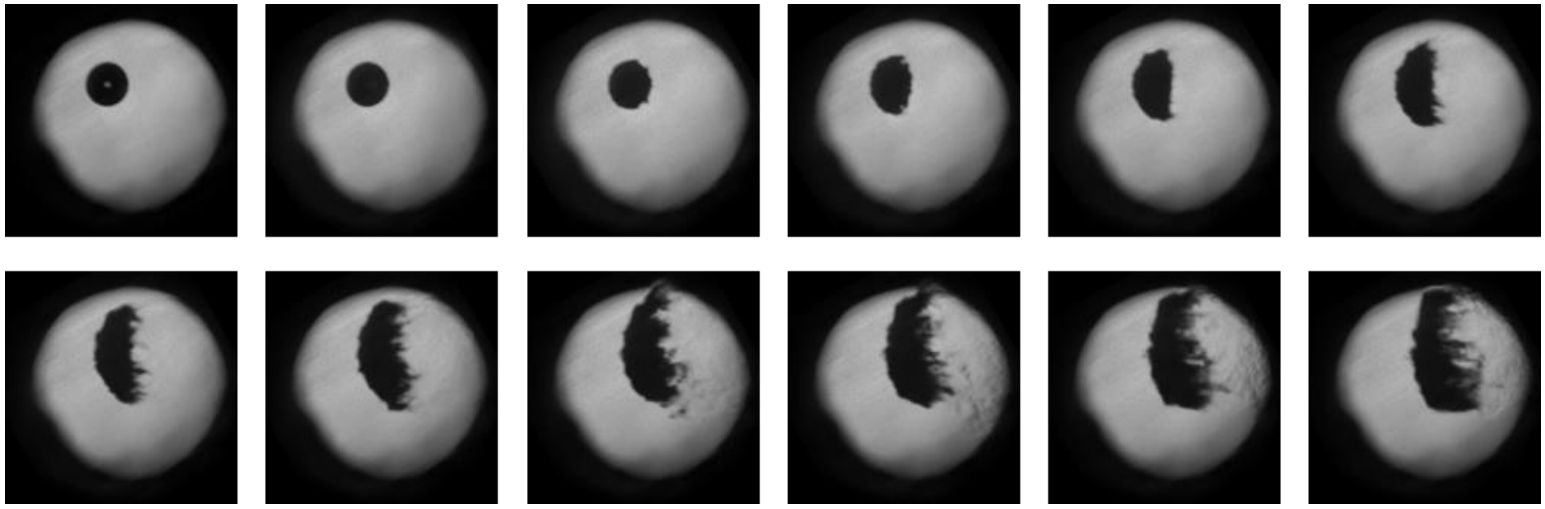

P_1 = 800 torr

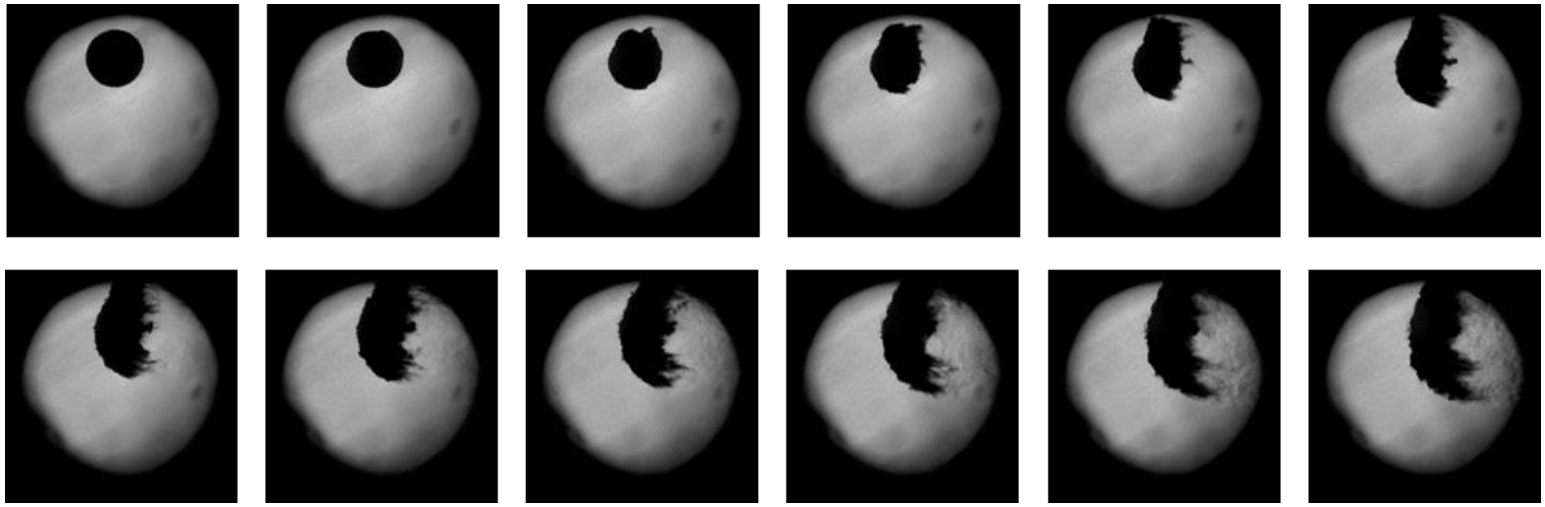

P_1 = 600 torr (1)

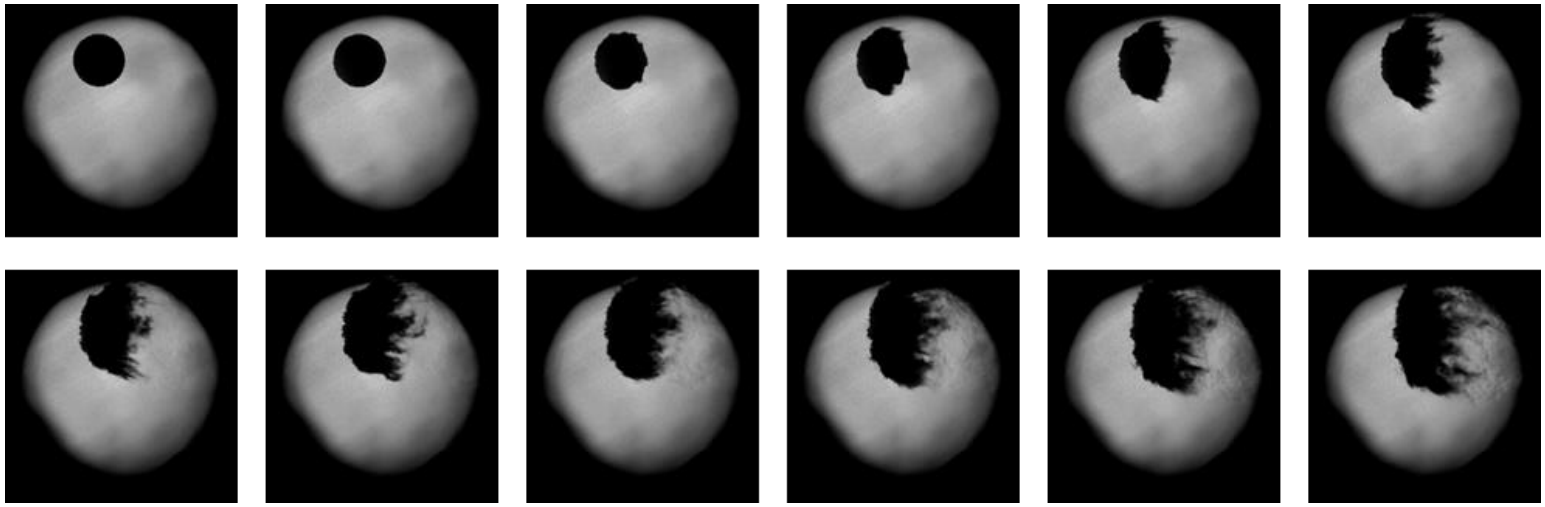

P_1 = 600 torr (2)

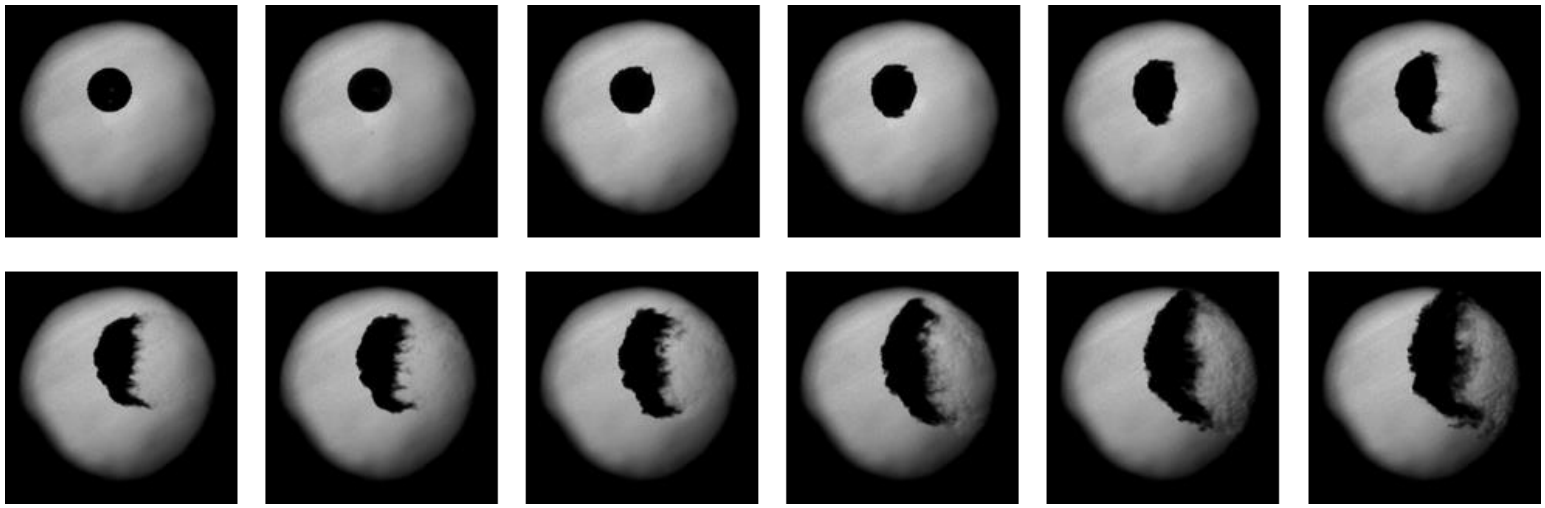

P_1 = 600 torr (DW speed deficit with CJ ~ 4%) (3)

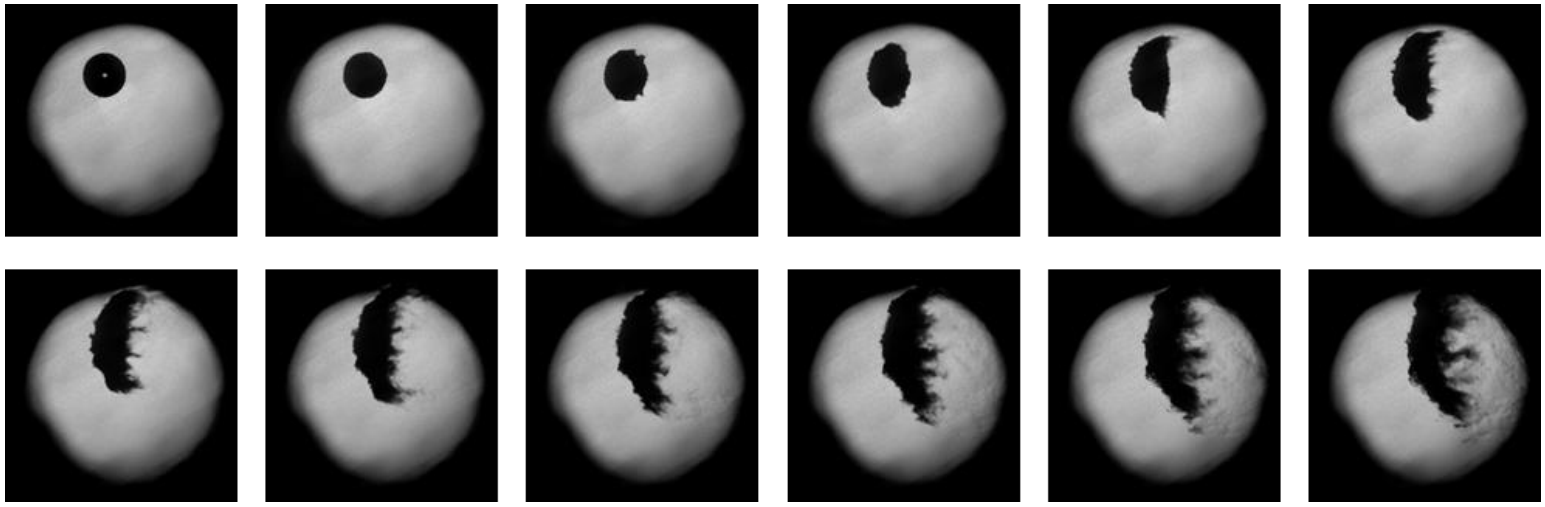

ER = 1.1 (1)

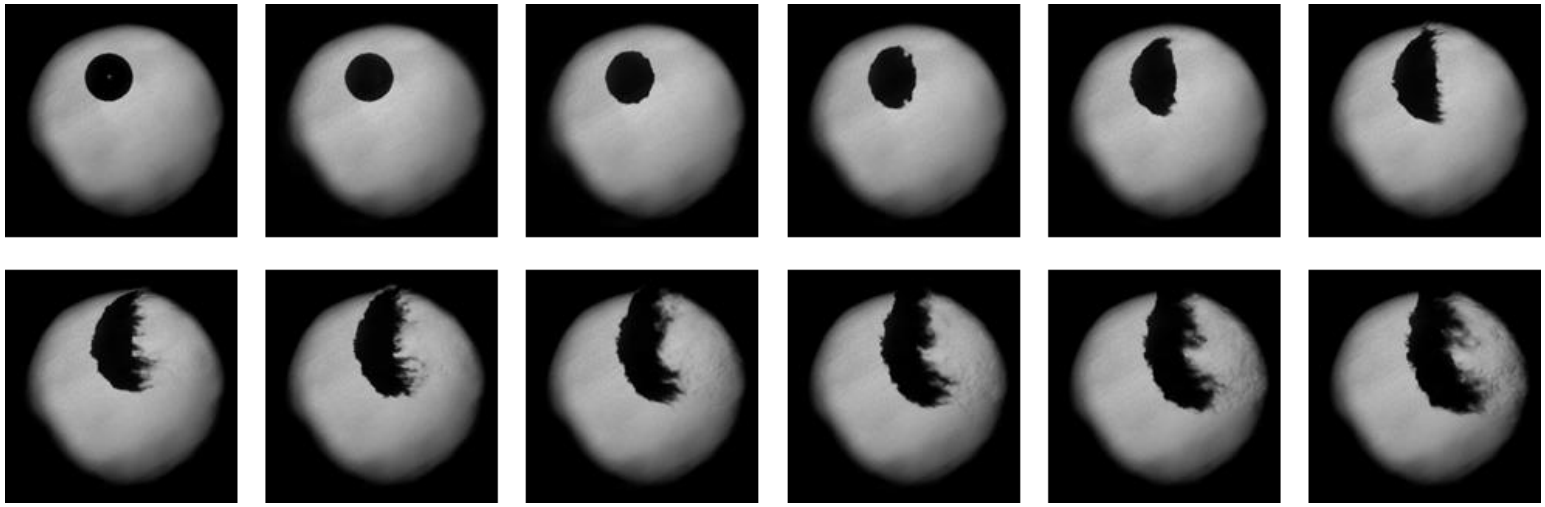

ER = 1.1 (2)

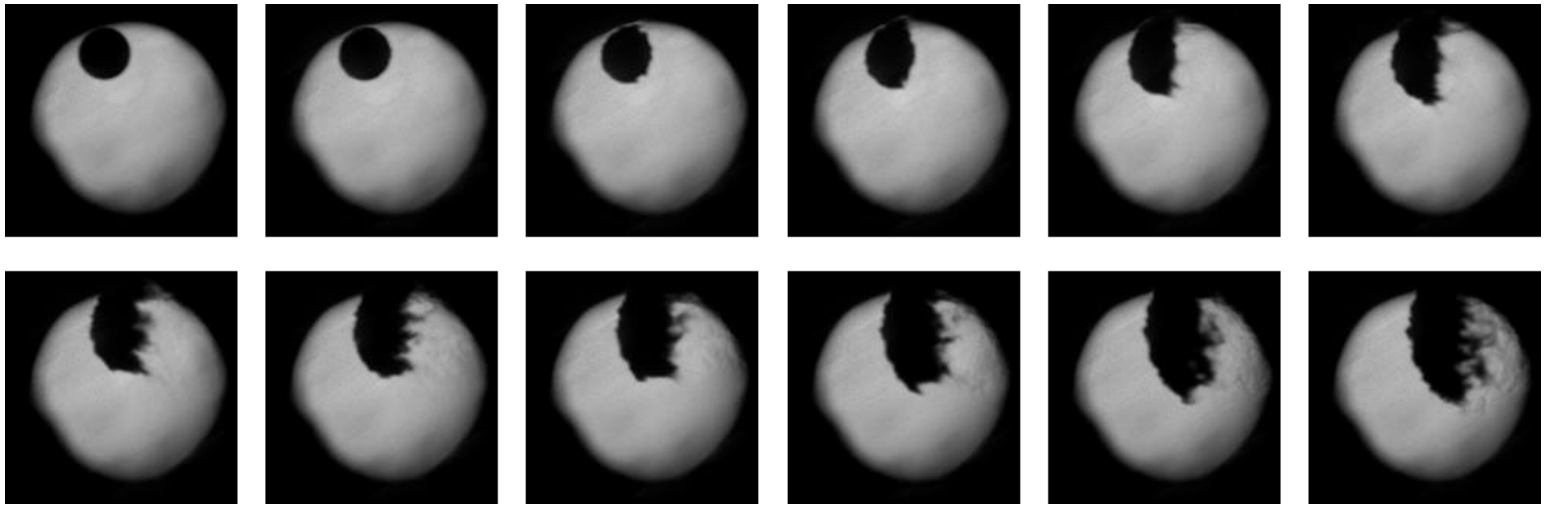

ER = 0.5 (1)

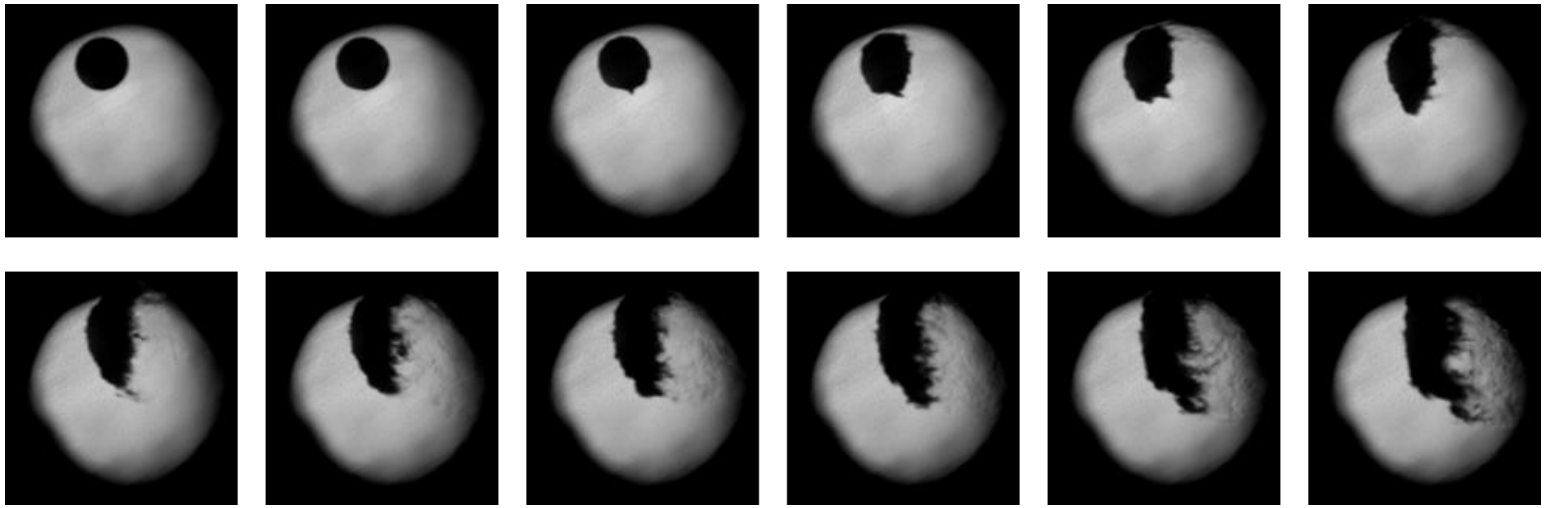

ER = 0.5 (2)

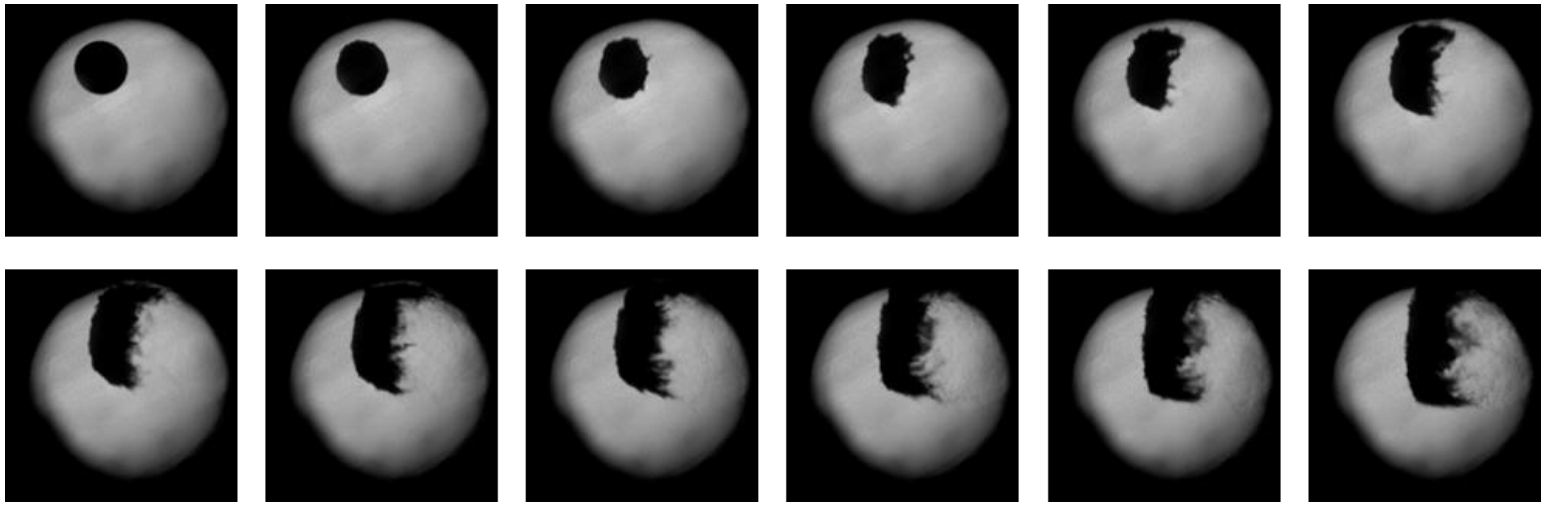

ER = 0.5 (3)

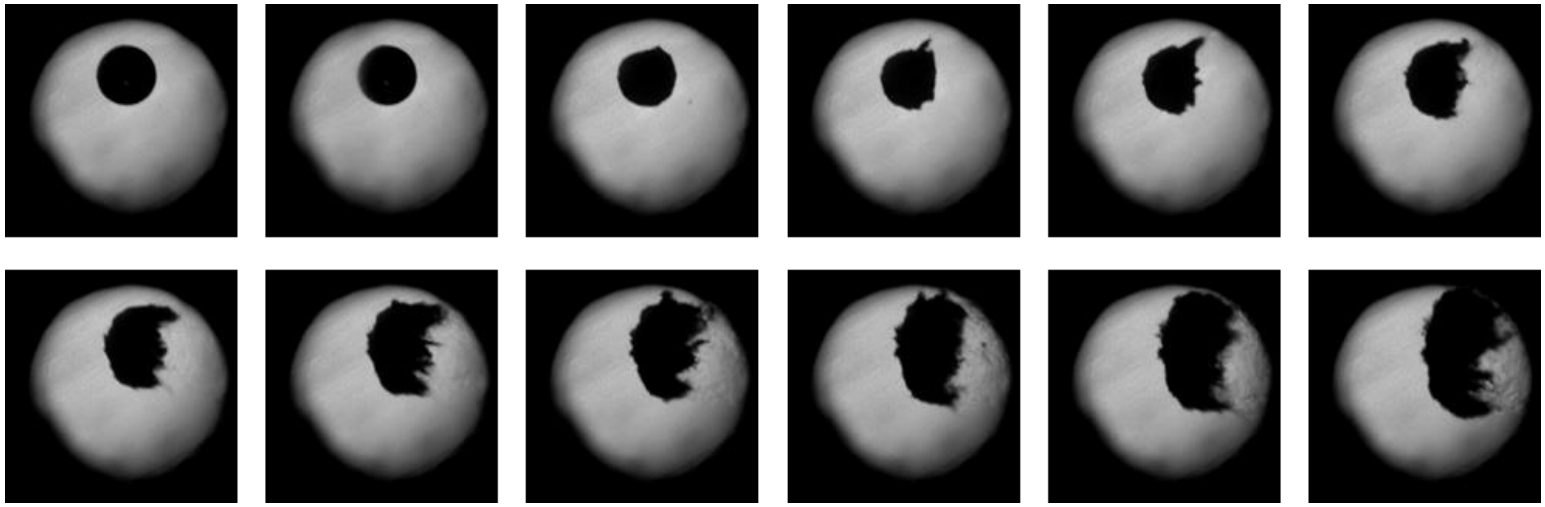

ER = 0.5 (4)

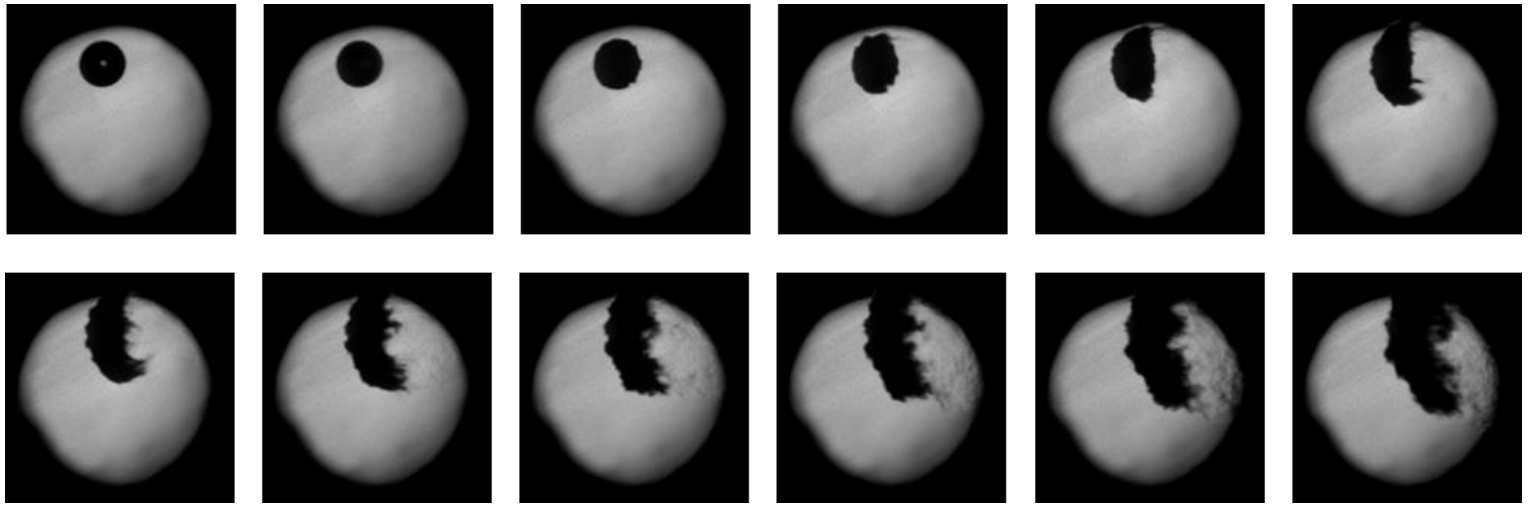

10% Argon (1)

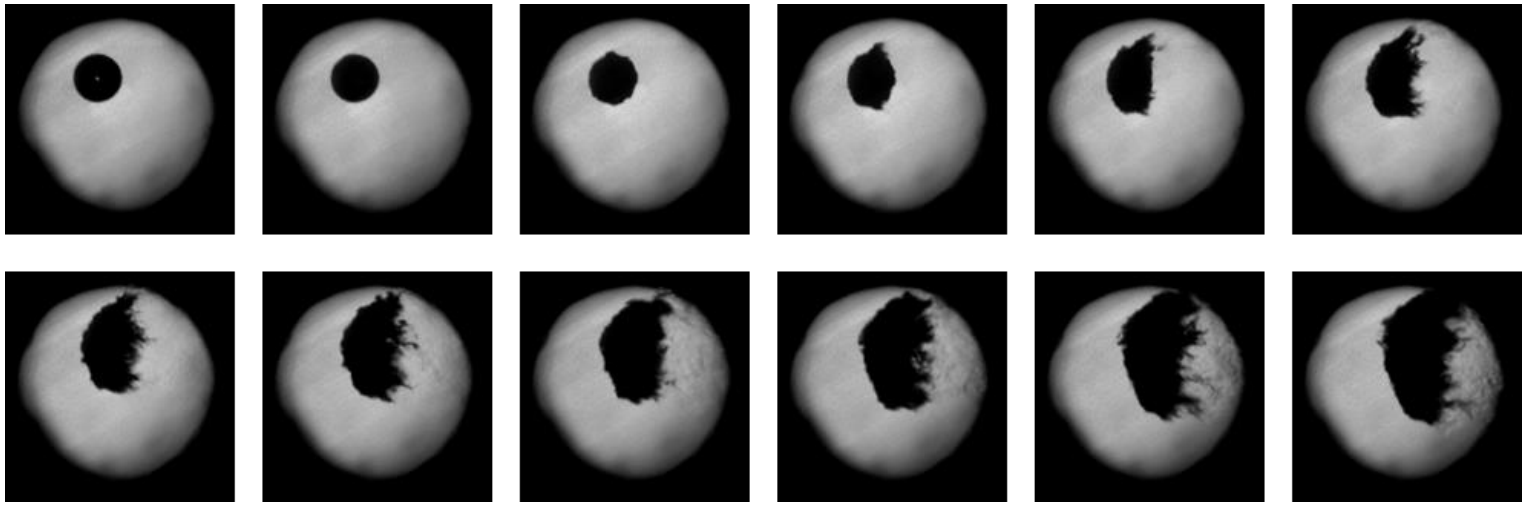

10% Argon (2)

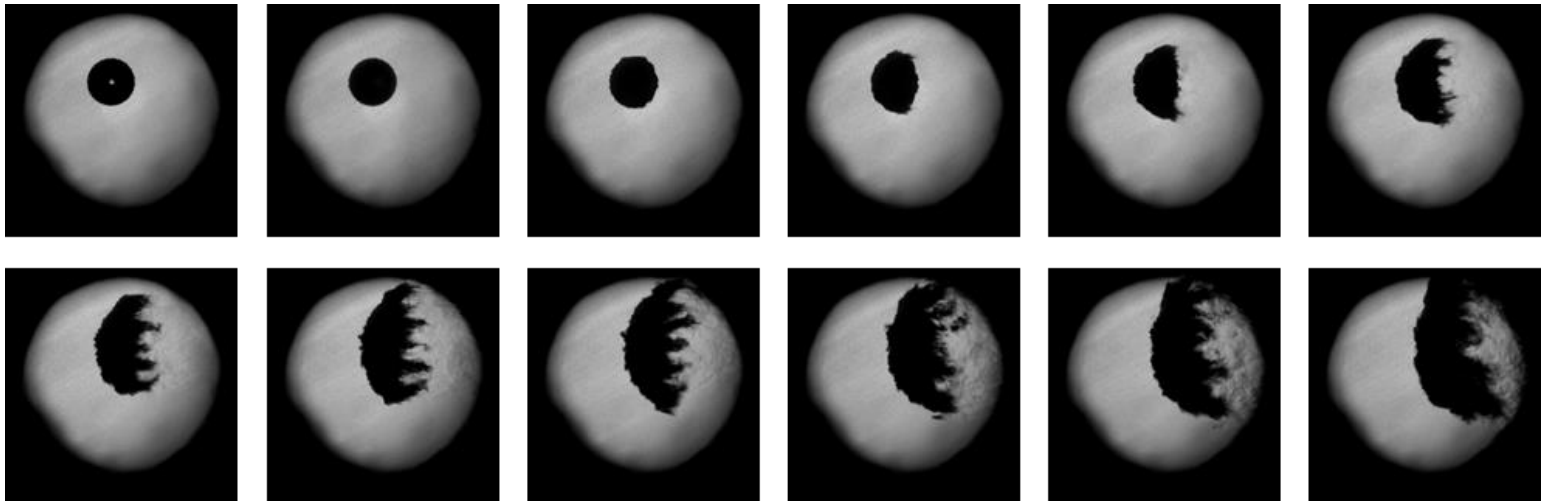

20% Argon (1)

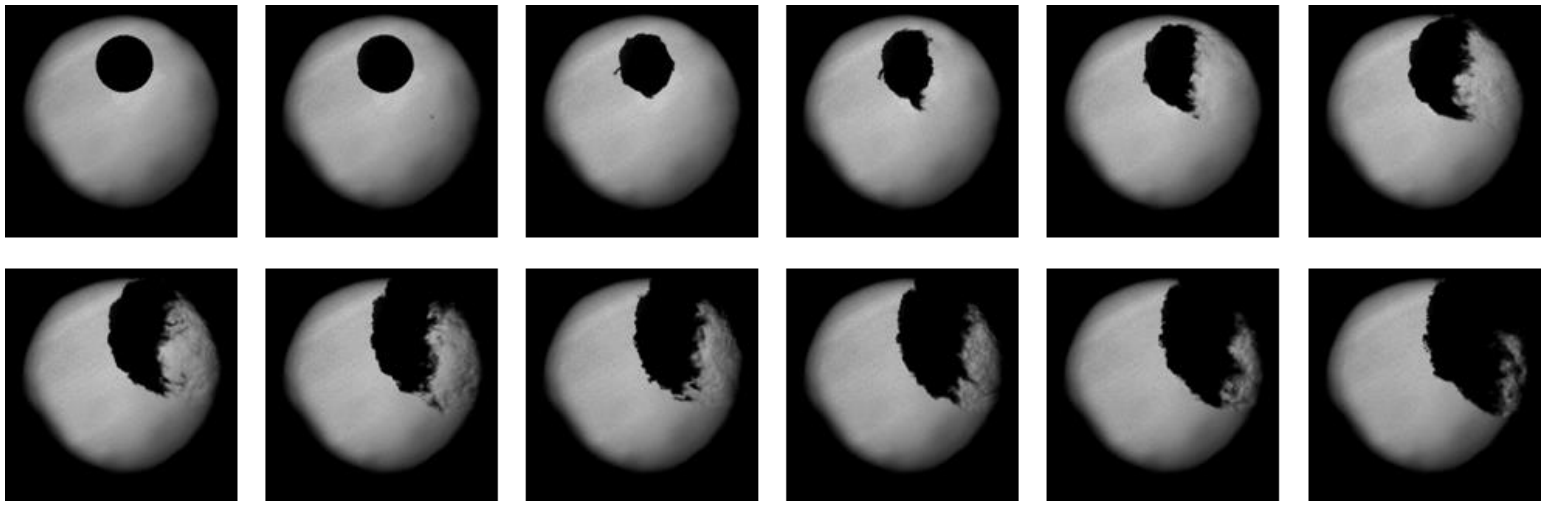

20% Argon (2)

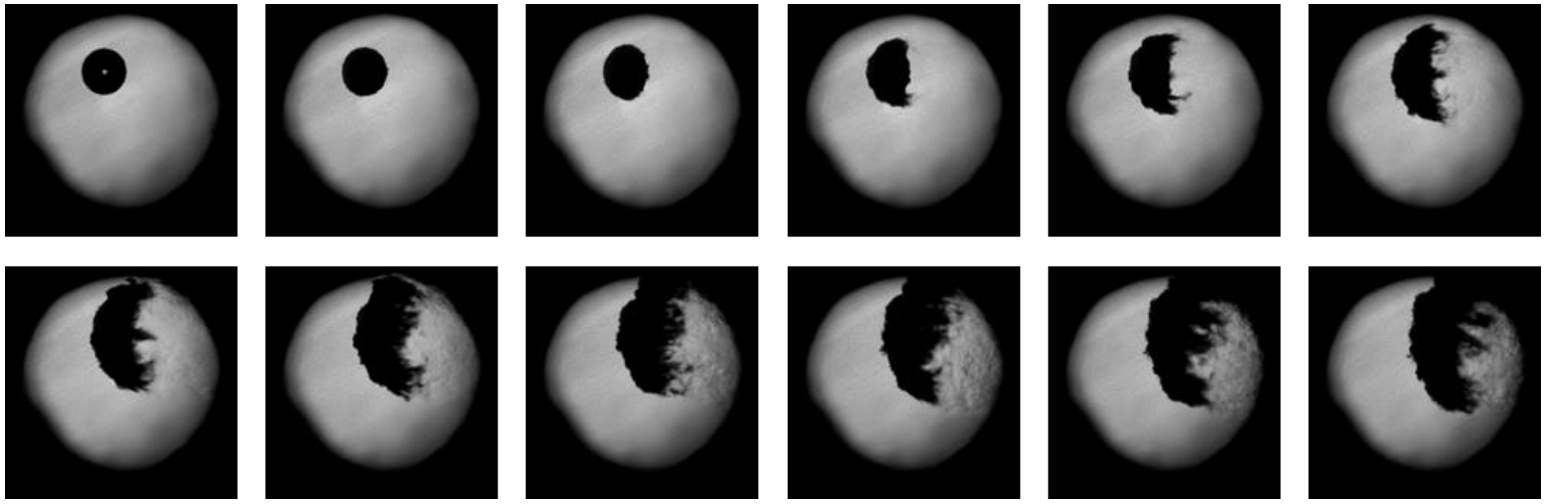

20% Argon (3)

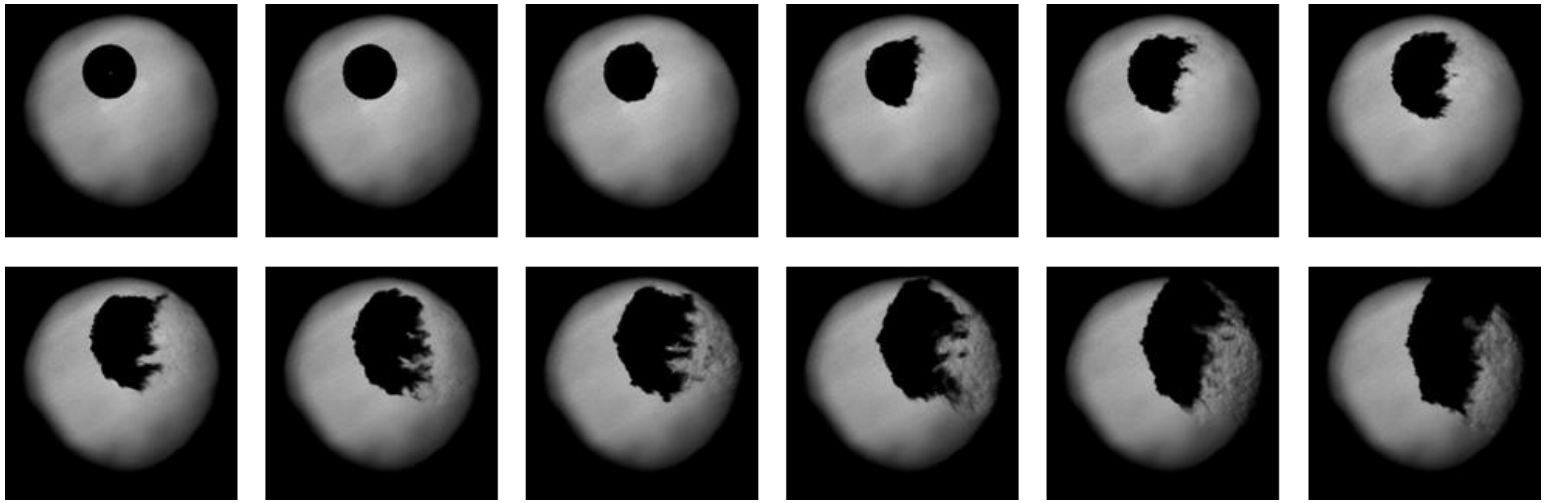

20% Argon (4)

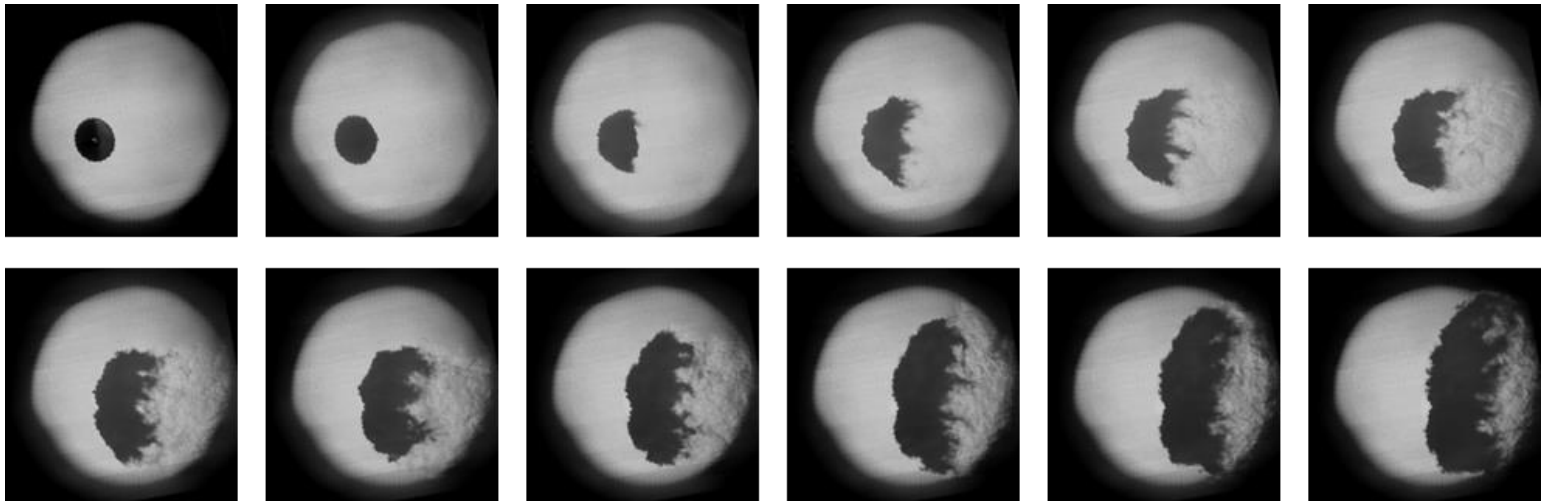

Methane (Diameter = 1.97 mm)

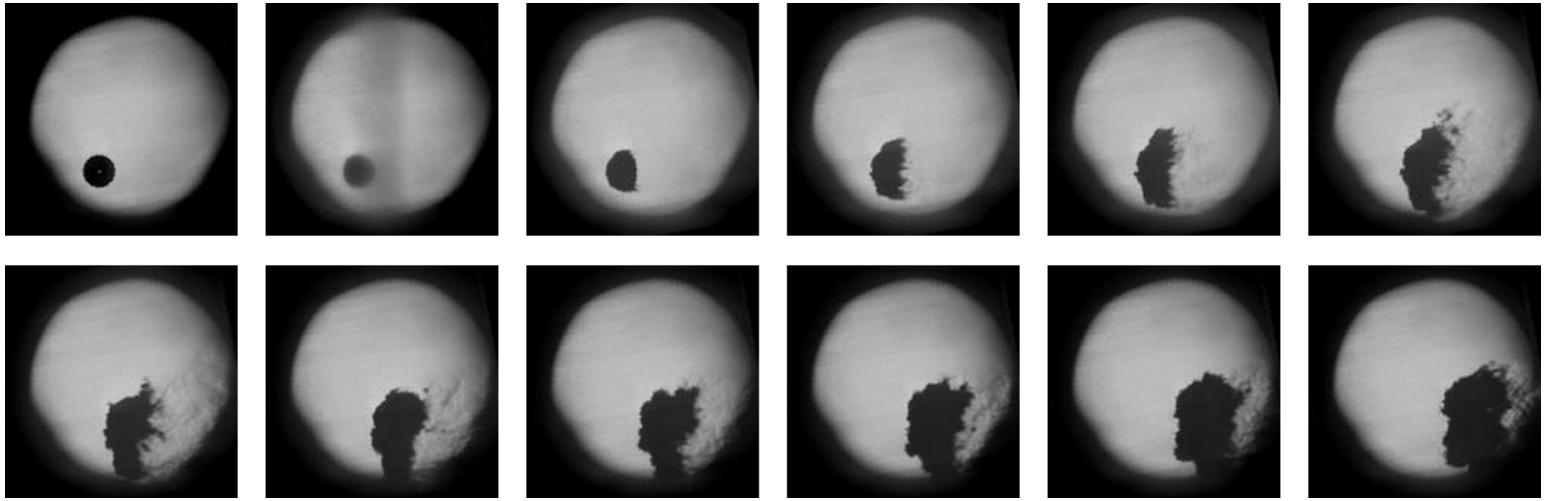

Methane (Diameter = 1.45 mm)

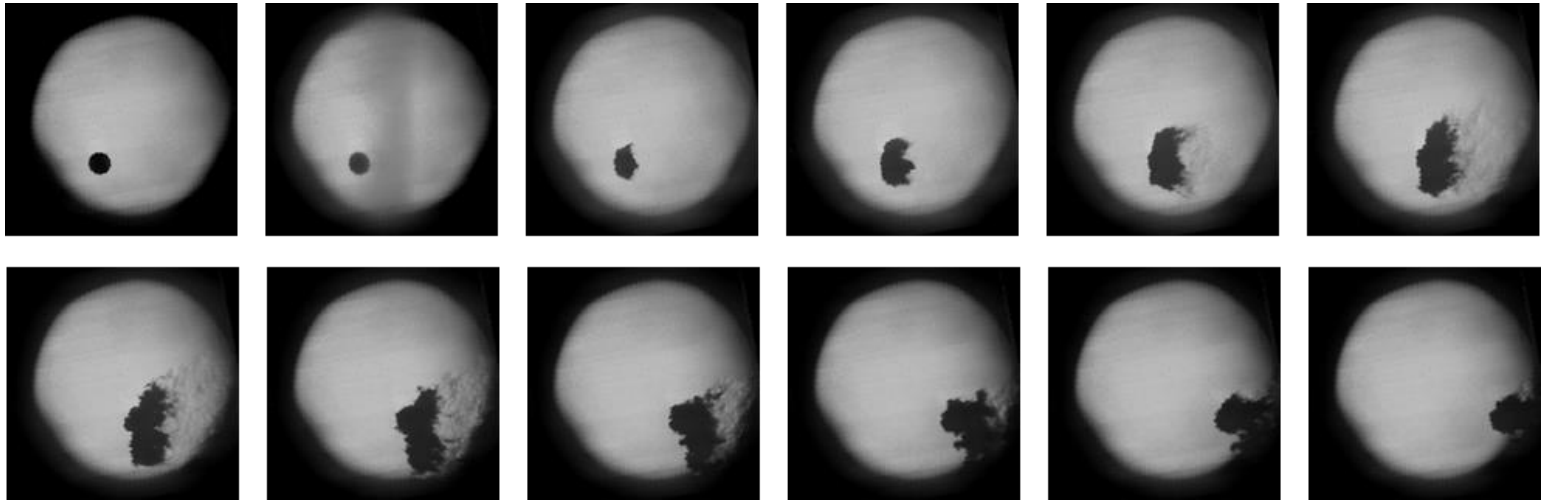

Methane (Diameter = 1.02 mm)

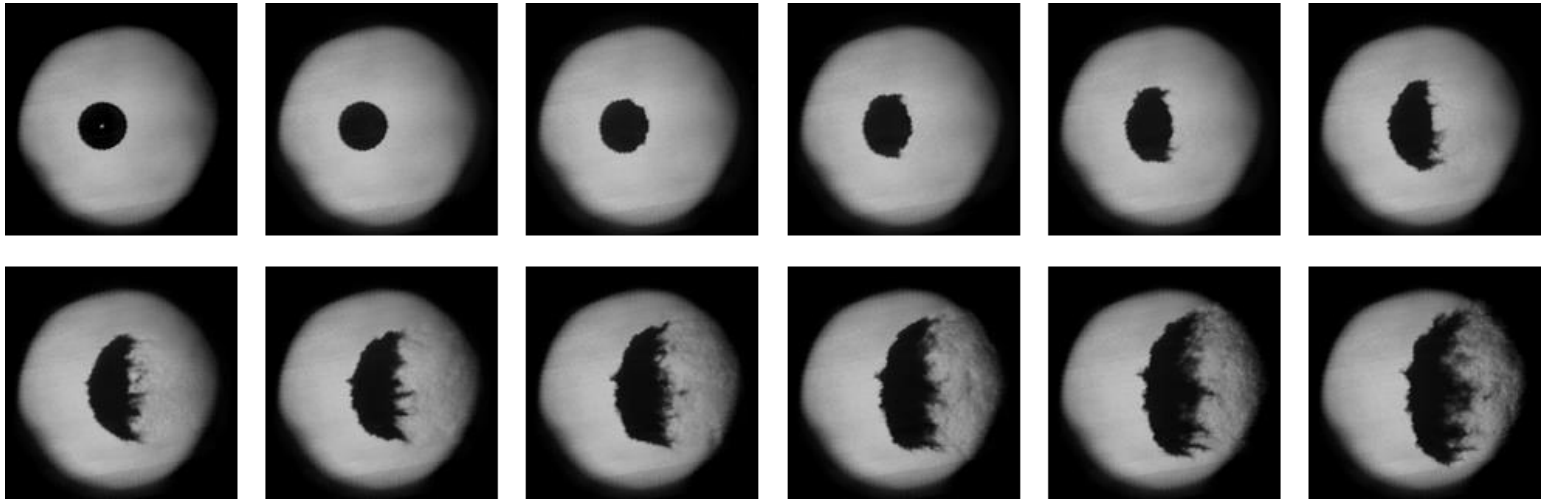

Water droplet

REFERENCES

[1] Gavrikov, A. I., Efimenko, A. A., and Dorofeev, S. B. "A model for detonation cell size prediction from chemical kinetics," *Combustion and Flame* Vol. 120, No. 1, 2000, pp. 19-33.
doi: https://doi.org/10.1016/S0010-2180(99)00076-0

[2] Clavin, P. "Nonlinear Dynamics of Shock and Detonation Waves in Gases," *Combustion Science and Technology* Vol. 189, No. 5, 2017, pp. 747-775.
doi: 10.1080/00102202.2016.1260562

[3] Nikolaev, Y. A., Vasil'ev, A. A., and Ul'yanitskii, B. Y. "Gas Detonation and its Application in Engineering and Technologies (Review)," *Combustion, Explosion and Shock Waves* Vol. 39, No. 4, 2003, pp. 382-410.
doi: 10.1023/A:1024726619703

[4] Soloukhin, R. I. "DETONATION WAVES IN GASES," *Soviet Physics Uspekhi* Vol. 6, No. 4, 1964, pp. 523-541.
doi: 10.1070/pu1964v006n04abeh003586

[5] Shepherd, J. E. "Detonation in gases," *Proceedings of the Combustion Institute* Vol. 32, No. 1, 2009, pp. 83-98.
doi: https://doi.org/10.1016/j.proci.2008.08.006

[6] Eckett, C. A. "Numerical and analytical studies of the dynamics of gaseous detonations." California Institute of Technology, Ann Arbor, 2001, p. 197.

[7] Heiser, W. H., and Pratt, D. T. "Thermodynamic Cycle Analysis of Pulse Detonation Engines," *Journal of Propulsion and Power* Vol. 18, No. 1, 2002, pp. 68-76.
doi: 10.2514/2.5899

[8] Schwer, D., and Kailasanath, K. "Fluid dynamics of rotating detonation engines with hydrogen and hydrocarbon fuels," *Proceedings of the Combustion Institute* Vol. 34, No. 2, 2013, pp. 1991-1998.
doi: https://doi.org/10.1016/j.proci.2012.05.046

[9] Rankin, B. A., Fotia, M. L., Naples, A. G., Stevens, C. A., Hoke, J. L., Kaemming, T. A., Theuerkauf, S. W., and Schauer, F. R. "Overview of Performance, Application, and Analysis of Rotating Detonation Engine Technologies," *Journal of Propulsion and Power* Vol. 33, No. 1, 2017, pp. 131-143.
doi: 10.2514/1.B36303

[10] Bennewitz, J. W., Bigler, B. R., Hargus, W. A., Danczyk, S. A., and Smith, R. D. "Characterization of Detonation Wave Propagation in a Rotating Detonation Rocket Engine using Direct High-Speed Imaging," *2018 Joint Propulsion Conference*.

[11] Kaplan, C. R., Özgen, A., and Oran, E. S. "Chemical-diffusive models for flame acceleration and transition-to-detonation: genetic algorithm and optimisation procedure," *Combustion Theory and Modelling* Vol. 23, No. 1, 2019, pp. 67-86.
doi: 10.1080/13647830.2018.1481228

[12] Lu, X., Kaplan, C. R., and Oran, E. S. "An efficient and accurate optimization method for the chemical-diffusive model," *Combustion and Flame* Vol. 232, 2021, p. 111517.

doi: https://doi.org/10.1016/j.combustflame.2021.111517
[13] Lu, X., Kaplan, C. R., and Oran, E. S. "A chemical-diffusive model for simulating detonative combustion with constrained detonation cell sizes," *Combustion and Flame* Vol. 230, 2021, p. 111417.
doi: https://doi.org/10.1016/j.combustflame.2021.111417
[14] Schwer, D. A., O'Fallon Jr, E., and Kessler, D. "Liquid-Fueled Detonation Modeling at the US Naval Research Laboratory." NAVAL RESEARCH LAB WASHINGTON DC WASHINGTON United States, 2018.
[15] Kailasanath, K., and Schwer, D. A. "High-Fidelity Simulations of Pressure-Gain Combustion Devices Based on Detonations," *Journal of Propulsion and Power* Vol. 33, No. 1, 2017, pp. 153-162.
doi: 10.2514/1.B36169
[16] Schwer, D., and Kailasanath, K. "Numerical investigation of the physics of rotating-detonation-engines," *Proceedings of the Combustion Institute* Vol. 33, No. 2, 2011, pp. 2195-2202.
doi: https://doi.org/10.1016/j.proci.2010.07.050
[17] Meng, Q., Zhao, N., and Zhang, H. "On the distributions of fuel droplets and in situ vapor in rotating detonation combustion with prevaporized n-heptane sprays," *Physics of Fluids* Vol. 33, No. 4, 2021, p. 043307.
doi: 10.1063/5.0045222
[18] Zhang, T., Sun, W., and Ju, Y. "Multi-scale modeling of detonation formation with concentration and temperature gradients in n-heptane/air mixtures," *Proceedings of the Combustion Institute* Vol. 36, No. 1, 2017, pp. 1539-1547.
doi: https://doi.org/10.1016/j.proci.2016.06.192
[19] Zhuang, Y., Li, Q., Dai, P., and Zhang, H. "Autoignition and detonation characteristics of n-heptane/air mixture with water droplets," *Fuel* Vol. 266, 2020, p. 117077.
doi: https://doi.org/10.1016/j.fuel.2020.117077
[20] Dabora, E. K., Ragland, K. W., and Nicholls, J. A. "Drop-size effects in spray detonations," *Symposium (International) on Combustion* Vol. 12, No. 1, 1969, pp. 19-26.
doi: 10.1016/s0082-0784(69)80388-7
[21] Nicholls, J. A., and Ranger, A. A. "Aerodynamic shattering of liquid drops," *AIAA Journal* Vol. 7, No. 2, 1969, pp. 285-290.
doi: 10.2514/3.5087
[22] Kauffman, C. W., Nicholls, J. A., and Olzmann, K. A. "The Interaction of an Incident Shock Wave with Liquid Fuel Drops," *Combustion Science and Technology* Vol. 3, No. 4, 1971, pp. 165-178.
doi: 10.1080/00102207108952284
[23] Ragland, K. W., Dabora, E. K., and Nicholls, J. A. "Observed Structure of Spray Detonations," *The Physics of Fluids* Vol. 11, No. 11, 1968, pp. 2377-2388.
doi: 10.1063/1.1691827
[24] Kauffman, C. W., and Nicholls, J. A. "Shock-wave ignition of liquid fuel drops," *AIAA Journal* Vol. 9, 1971, p. 880.
doi: 10.2514/3.6290
[25] Guildenbecher, D. R., López-Rivera, C., and Sojka, P. E. "Secondary atomization," *Experiments in Fluids* Vol. 46, No. 3, 2009, pp. 371-402.

doi: 10.1007/s00348-008-0593-2
[26] Joseph, D. D., Belanger, J., and Beavers, G. S. "Breakup of a liquid drop suddenly exposed to a high-speed airstream," *International Journal of Multiphase Flow* Vol. 25, No. 6, 1999, pp. 1263-1303.
doi: https://doi.org/10.1016/S0301-9322(99)00043-9
[27] Theofanous, T. G., and Li, G. J. "On the physics of aerobreakup," *Physics of Fluids* Vol. 20, No. 5, 2008, p. 052103.
doi: 10.1063/1.2907989
[28] Theofanous, T. G. "Aerobreakup of Newtonian and Viscoelastic Liquids," *Annual Review of Fluid Mechanics* Vol. 43, No. 1, 2011, pp. 661-690.
doi: 10.1146/annurev-fluid-122109-160638
[29] Theofanous, T. G., Mitkin, V. V., Ng, C. L., Chang, C.-H., Deng, X., and Sushchikh, S. "The physics of aerobreakup. II. Viscous liquids," *Physics of Fluids* Vol. 24, No. 2, 2012, p. 022104.
doi: 10.1063/1.3680867
[30] Sharma, S., Pratap Singh, A., Srinivas Rao, S., Kumar, A., and Basu, S. "Shock induced aerobreakup of a droplet," *Journal of Fluid Mechanics* Vol. 929, 2021, p. A27.
doi: 10.1017/jfm.2021.860
[31] Kailasanath, K. "Liquid-fueled detonations in tubes," *J. Propulsion Power* Vol. 22, 2006, pp. 1161-1168.
doi: 10.2514/1.19624
[32] Saretto, S., Lee, S.-Y., Conrad, C., Brumberg, J., Pal, S., and Santoro, R. "Predetonator to Thrust Tube Detonation Transition Studies for Multi-Cycle PDE Applications," *39th AIAA/ASME/SAE/ASEE Joint Propulsion Conference and Exhibit*. 2003.
[33] Browne, S., Ziegler, J., and Shepherd, J. "Numerical solution methods for shock and detonation jump conditions," *GALCIT report FM2006* Vol. 6, 2008, p. 90.

[34] Ragland, K. W., Bryden, K. M., and Kong, S.-C. *Combustion engineering*: CRC press Boca Raton, FL, 2011.
[35] Meng, J. C., and Colonius, T. "Numerical simulation of the aerobreakup of a water droplet," *Journal of Fluid Mechanics* Vol. 835, 2018, pp. 1108-1135.
doi: 10.1017/jfm.2017.804
[36] O'Rourke, P. J., and Amsden, A. A. "The TAB method for numerical calculation of spray droplet breakup," *Conference: International fuels and lubricants meeting and exposition, Toronto, Canada, 2 Nov 1987; Other Information: Portions of this document are illegible in microfiche products*. United States, 1987, p. Medium: ED; Size: Pages: 12.
[37] Hsiang, L. P., and Faeth, G. M. "Drop deformation and breakup due to shock wave and steady disturbances," *International Journal of Multiphase Flow* Vol. 21, No. 4, 1995, pp. 545-560.
doi: https://doi.org/10.1016/0301-9322(94)00095-2